Project 055 Noise Generation and Propagation from Advanced Combustors

Georgia Institute of Technology
RTX Technology Research Center

Project Lead Investigator

Timothy Lieuwen
Professor
Daniel Guggenheim School of Aerospace Engineering
Georgia Institute of Technology
270 Ferst Drive (M/C 0150)
Atlanta, GA 30332-0150
404-894-3041
tim.lieuwen@aerospace.gatech.edu

University Participants

Georgia Institute of Technology (Georgia Tech or GT)

- P.I.s: Prof. Timothy Lieuwen, Prof. Suresh Menon, Dr. Vishal Acharya, Dr. Benjamin Emerson
- FAA Award Number: 13-C-AJFE-GIT-058
- Period of Performance: February 5, 2020, to December 31, 2026
- Tasks:
  1. GT Experiments: This task addresses the measurements from experiments that will be performed at Georgia Tech. The task involves coordination between the teams to develop and define the aerodynamic design of a rich-quench-lean (RQL), quick quench, lean burn combustor for this study. This task is led by Tim Lieuwen with support from Ben Emerson and David Wu.
  2. GT Simulations: This task includes simulating the experiment at RTRC, with a focus on the pre-combustion flow dynamics, flame dynamics, and post-combustion dynamics of pressure and entropy disturbances. This task is led by Suresh Menon.
  3. GT Reduced-Order Modeling: This task consists of creating a reduced-order model (ROM) framework for the unsteady response of the flame and the generation of entropy disturbances due to unsteady heat release. This task is led by Vishal Acharya.

RTX Technology Research Center (RTRC)

- P.I.s: Dr. Jeffrey Mendoza, Dr. Duane McCormick, Dr. Julian Winkler, Dr. Lance Smith
- FAA Award Number: 13-C-AJFE-GIT-058 (subaward through Georgia Tech)
- Period of Performance: February 5, 2020, to December 31, 2026
- Tasks:
  4. RTRC Facility Development: This task addresses the design of experiments that will be performed at RTRC. The task involves coordination between the teams to develop and define the aerodynamic design of an RQL combustor for this study. This task is led by Jeffrey Mendoza, Lance Smith, and Duane McCormick.
  5. RTRC Post-Combustion Modeling: This task consists of both post-processing and simulation efforts. First, the post-combustion simulation data from the simulation of the Georgia Tech experiment are mined to investigate the dynamics of entropy fluctuations and their transport. Next, simulations are used to model noise propagation in the post-combustion architecture of the engine. The simulations are split across the different sections: nozzle, turbine, and far-field. This task is led by Jeffrey Mendoza and Julian Winkler.

Project Funding Level

Federal Aviation Administration (FAA) Funding: $4,999,984 (Georgia Tech: $3,000,343; RTRC: $1,999,641)

Cost-Share Funding: $4,772,851 (Georgia Tech: $2,773,210 from Airspace Engineering (AE) school; RTRC: $1,999,641 from company funds)
Total Funding: $9,772,835

Investigation Team

Georgia Institute of Technology

Prof. Tim Lieuwen, (P.I.), Lead P.I. responsible for overseeing all tasks; specifically, he leads the Georgia Tech experiments and design in Tasks 1 and 2, along with Prof. Steinberg. In addition, he co-leads the modeling tasks in Task 1 for pre-combustion, flame response, and post-combustion modeling, along with Dr. Acharya.

Prof. Suresh Menon, (co-P.I.), Responsible for simulations of the Georgia Tech experiment.

Dr. Vishal Acharya, (co-P.I.; Principal Research Engineer), Responsible for all modeling tasks for pre-combustion, combustion, and post-combustion physics, along with Professor Lieuwen. In addition, as an administrative coordinator, he is responsible for general project management, such as project deliverables, group meetings, and interfacing with the FAA project manager.

Dr. Benjamin Emerson, (co-P.I.; Principal Research Engineer), Responsible for designing and maintaining experimental facilities, as well as experimental operations and management, and graduate students' safety.

Dr. Achyut Panchal, (Research Engineer), Simulation of the Georgia Tech experiment.

Sungyoung Ha, (graduate student), Lead experimentalist on the Georgia Tech rig.

Parth Patki, (graduate student), Working on hydrodynamics modeling subtask (pre-combustion disturbances).

Guru Charan Ganesh, (graduate student), Working on the entropy dynamics modeling subtask (post-combustion disturbances).

Leo M. Kastenberg (graduate student), Working on analysis of large eddy simulation (LES) results and responsible for setting new simulations (until July 2025).

Sathvik Gujjati (graduate student), Working on analysis of large eddy simulation (LES) results and responsible for setting new simulations (since August 2025).

RTX Technology Research Center

Dr. Jeffrey Mendoza, (P.I.; Technical Fellow Acoustics), Leads the RTRC team and oversees its contributions to the project. He leads the subtasks related to modeling, measurements, and simulation for post-combustion disturbances, nozzle interactions, turbine interactions, and far-field sound propagation.

Dr. Lance Smith, (co-P.I.; Technical Fellow Combustion), Conducting design and measurements of the RTRC experiment. He collaborates closely with the Georgia Tech team to ensure similarities between both experiment setups.

Dr. Duane McCormick, (co-P.I.; Principal Research Engineer), Conducting design and measurements of the RTRC experiment as well as finite-element calculations in the design process.

Dr. Julian Winkler, (co-P.I.), Responsible for the simulation tasks at RTRC and focuses on post-combustion disturbances, nozzle interactions, turbine interactions, and far-field sound propagation.

Dr. Jordan Snyder, conducting design, measurements, and data processing using tunable diode laser absorption spectroscopy and chemiluminescence in the RTRC combustor rig.

Dr. Kenji Homma, Responsible for far-field sound propagation simulations.

Dr. Aaron Reimann, Responsible for ROM and high-fidelity (HiFi) modeling of the propagation of direct and indirect noise sources through the turbine nozzle and supports the far-field sound propagation simulations.

Dr. Sudarshan Koushik, Responsible for post-processing the Georgia Tech LES data to model post-combustion disturbances.

Project Overview

The objective of this project is to develop and validate physics-based design tools that can predict noise production mechanisms and their relative dominance and ultimately reduce the noise output of future engines. The motivation for this project stems from recent and future advances in aircraft engine technology. High-bypass engine technology has significantly reduced the traditionally dominant engine noise sources, namely fan and jet exhaust noise. Noise generated in the combustor has become a dominant source of engine noise for future advanced aircraft designs. In addition, as combustors evolve to increase efficiency and decrease pollutant emissions, methods for predicting and mitigating combustion noise have severely lagged, and legacy methods are insufficient to predict noise from next-generation combustors. This drawback has motivated the objective of this project, which addresses the critical need for physics-based

design tools. The resultant understanding of noise generation and propagation, along with validated noise prediction tools, will enable more rapid and cost-effective designs of low-noise engines for future aircraft.

The project objectives will be achieved through a program of cooperative experiments, high-fidelity simulations, and physics-based ROM. The physical processes involved are tightly coupled and directly determine the project tasks, as shown in Figure 1.

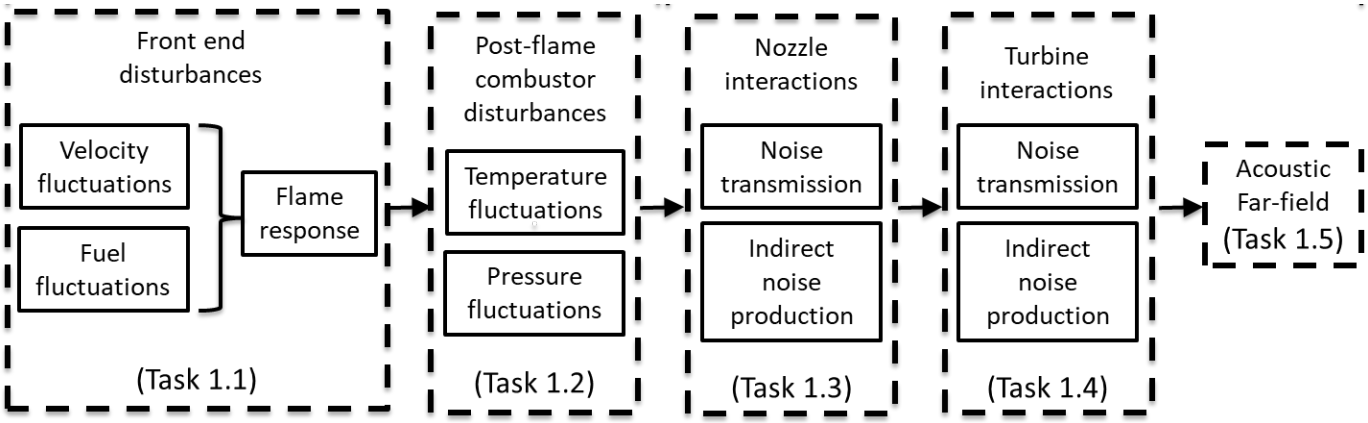

Figure 1. Diagram showing physical processes and project tasks for noise generation.

The physics of noise generation begins with source disturbances upstream of the combustion zone, which involve unsteady dynamics in the flow and incoming fuel (spray), followed by the response of the combustion zone (flame) to these upstream disturbances. The fluctuations in the unsteady heat release led to the generation of pressure and entropy fluctuations. These fluctuations propagate further downstream in the combustor, interact with the nozzle and turbine, and eventually lead to far-field sound generation. Given the complex interplay of unsteady physics in the various parts of the engine, developing a ROM is challenging.

An important goal of this project is to generate high-quality reference data from both measurements and validated high-fidelity simulations, including measurements of the flow, spray, and flame unsteadiness in the head end of the combustor. Subsequently, the secondary combustion zone is characterized. The generation of entropy and pressure disturbances is then characterized by measurements of temperature and pressure fluctuations, followed by measurements of noise reflection and transmission through the turbine and nozzle section, and sound measurements in the far field. The measurements are accompanied by LES and finite-element simulations that are validated against the measurements. Collectively, these data are generated across a range of operating parameters and provide a source database for the modeling task.

The main goal of this project is to develop a robust design tool that can predict noise at operating points for which prior measurements or data are unavailable. To achieve this goal, two major tasks are necessary. First, ROM and frameworks must be developed for various aspects of the engine architecture: flow/spray models, flame response models, entropy generation models, entropy propagation models, nozzle interaction models, turbine interaction models, and far-field noise generation models. The ROM for each of these aspects involves simplifications and assumptions that are validated against the source database. The validation study and iterative improvement of model predictions serve as the second task to achieve this goal.

In this report, the efforts of both teams, Georgia Tech and RTRC, are summarized from October 2024 to September 2025. The efforts primarily include Georgia Tech rig setups to ascertain the coherence of pressure and heat release fluctuations in both open and ducted flames. The RTRC rig was used to study the effect of tonal noise through a combination of measurements and finite element method (FEM) simulations. In addition, progress was made in hydrodynamics modeling, direct noise modeling and entropy noise modeling.

Task 1 – GT Experiments

Georgia Institute of Technology

Objective

The Georgia Tech experimental team has performed detailed studies on heat release – pressure coherence using the open flame rig developed in the previous period. With some modifications, high quality data have been obtained which allowed a systematical study on coherence, both confirming prior model predictions and highlighting new areas of study. The experiment was further expanded to a ducted configuration, which also supplemented modelling studies performed in the previous period.

Research Approach

Experimental Rig and Methods

The turbulent Bunsen burner that was constructed in the previous period was used in this period as well, with a few upgrades to the diagnostics. To reiterate, the burner is a piloted Bunsen burner using a blend of methane and air which are metered and controlled independently through critical orifices. A muffler and turbulence generator prior to the nozzle mitigates upstream flow noise, particularly from the orifices, and gives some control over the turbulence intensity. Acoustic data were taken through a PCB® Piezotronics 378B02 free-field microphone. A Photron® FASTCAM SA-Z1 high speed camera paired with a Lambert™ HiCATT intensifier was used to take high speed images of the flame, and three Thorlabs® PMM01 photomultiplier tubes were used to obtain global chemiluminescence intensity measurements. The configuration of the rig and diagnostics are shown in Figure 2.

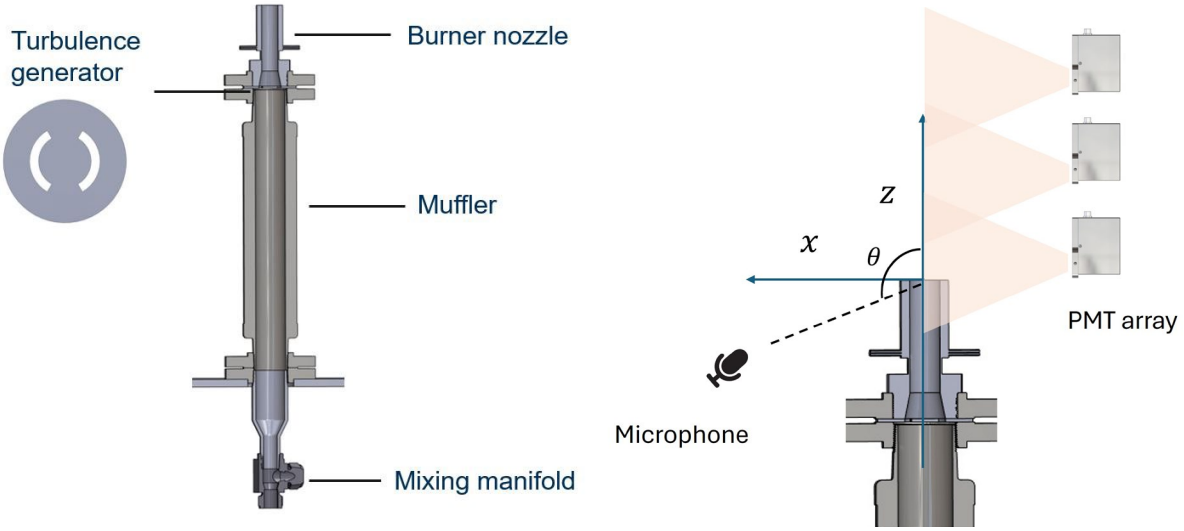

Figure 2. Cross section of experimental apparatus (left) and schematic of diagnostics (right). PMT: photomultiplier tube.

In the previous period, it was determined that the noise in photomultiplier tube (PMT) measurements limited the ability to resolve coherence at higher frequencies. Several modifications and efforts were made to improve the quality of PMT measurements. First, the filter was replaced with an edgepass filter with a nominal transmission window of 400 nm – 444 nm. This relatively wider bandwidth allows a stronger signal mainly composed of CH* emissions and the hydrocarbon continuum which is predominantly CO_2* emissions. While there are some differences in the characteristics of CH* and CO_2* emissions, the correlation between the heat release rate and chemiluminescence is expected to be high for the flame used

® PCB is a registered trademark of PCB Piezotronics, Inc., Depew, New York.
® Photron is a registered trademark of Photron Limited, Tokyo, Japan.
™ Lambert instruments is a trademark of Tibidabo Scientific Industries, Madison, Connecticut.
® Thorlabs is a registered trademark of Thorlabs, Inc., Newton, New Jersey.

in this study. Additional care was taken to minimize external lighting by coordinating with facility management to turn off the facility lights during testing and conducting experiments at night after sunset. To further minimize the effect of emergency lights that could not be turned off and reflections, a black background was installed.

The improvement of signal through these methods is shown in Figure 3, where the coherence between two PMT measurements with the same viewing window is shown for a benchmark case. It is difficult to estimate the noise floor in PMT signals with background measurements as PMT noise not only includes a background component but also shot noise which scales with the input signal. By taking the coherence between two PMT measurements which have the same viewing window, it is possible to estimate the effect of all noise sources and establish an upper limit on the measurable coherence. The coherence limit is increased with each improvement effort, and eventually there is no drop in coherence due to PMT measurement noise up to approximately 1kHz.

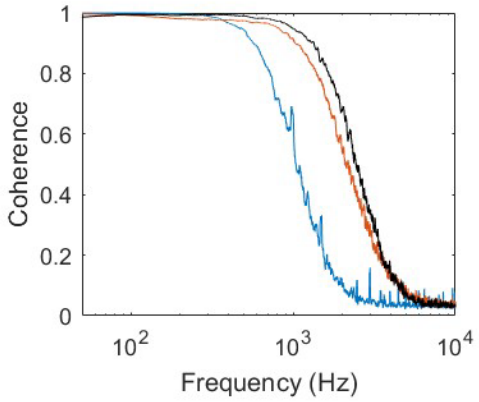

Figure 3. Coherence of two PMT measurements with the new filter (blue), also with the facility lights off (orange), and with the backdrop (black).

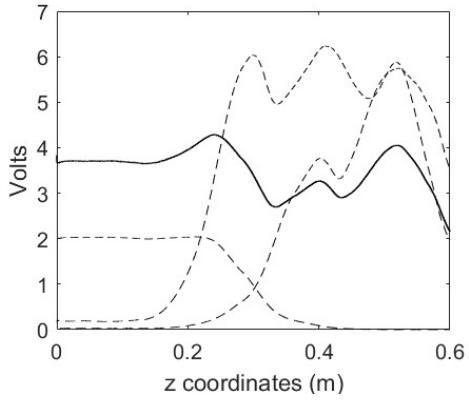

Figure 4. Spatial transfer function of individual PMTs shown by a dashed line and corrected spatial transfer function of the PMT array shown by a solid line.

It is also important to ensure that the PMT viewing window covers the entire flame to capture the global chemiluminescence. While it is desired to place the PMT close to the flame as possible to maximize signal intensity, this also limits the viewing window of the PMT. To find a balance between this tradeoff, three PMTs were arranged in a vertical array as shown in Figure 2 to allow sufficient coverage while also maintaining proximity to the flame. The spatial transfer function of each PMT was calculated by translating a constant point light source. Then the coefficients were calculated

where a linear sum of the PMT signals will yield a constant spatial transfer function. The global chemiluminescence intensity was calculated by summing the PMT signals according to this correction. This process is shown in Figure 4.

To measure coherence and its roll-off characteristics, it is desirable for the flame to have broadband characteristics, to be well anchored so that it does not lift off, and to have an appropriately long flame length such that good measurement accuracy is achieved for a wide range of κL_f values, where κ is the acoustic wavenumber and L_f is the flame length. The operating conditions shown in Table 1 were selected to achieve such conditions. Cases A indicates cases without the turbulence generator and Cases B are cases with the turbulence generator.

Table 1. Operating conditions for experiment.

Label	Air flow rate (g/s)	Fuel flow rate (g/s)	Average nozzle velocity (m/s)	Equivalence Ratio	R_e (×10⁴)	$L_{f_{90}}$ (cm)
A1, B1	14.8	1.05	20.2	1.23	3.85	26.6, 32.7
A2, B2	14.4	1.14	19.9	1.36	3.79	39.5, 38.5
A3, B3	15.2	1.22	21.0	1.38	4.00	38.2, 38.0
A4	11.1	0.81	15.1	1.26	2.88	29.6
A5	11.1	0.64	14.7	1.00	2.82	16.0
B4	8.8	0.60	11.9	1.18	2.28	26.7
B5	6.0	0.41	8.2	1.18	1.56	18.3
A6*, B6*	14.8	0.89 - 1.46	19.8- 21.0	1.04 - 1.70	3.78 - 4.00	--
B7*	8.8	0.56 - 0.97	11.8- 12.7	1.10 - 1.90	2.26 - 2.42	--
B8*	1.8	0.40 - 0.81	15.2 - 19.7	3.88 - 7.88	2.50 - 3.20	--

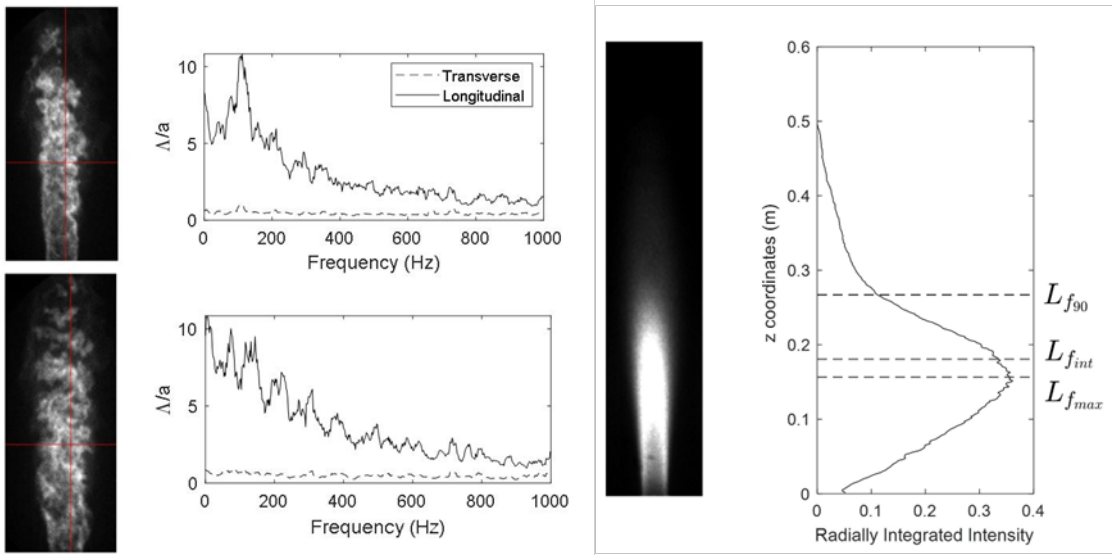

Figure 5. Normalized flame correlation length calculated from high-speed images for Cases A1 (upper left) and B1 (lower left), and mean chemiluminescence image and axial heat release rate distribution (right).

High speed camera images were used to calculate the flame correlation length, and mean images were used to derive the flame length. The flame correlation length is a key parameter that describes the spatiotemporal statistics of the heat release, which is defined as $\Lambda(x, e_r) = \int_0^\infty \frac{2}{\pi^{1/2}} \frac{|\langle q_v(x) q_v(x+r) \rangle|}{\langle q_v(x)^2 \rangle} dr$. Figure 5 shows how these images are processed. The correlation length in the longitudinal (along the flow) direction is greater than the transverse direction, showing the convective nature of the flame. It should be noted that model results predict that a correlation length variation in this range has an insignificant effect on coherence. The flame length is determined from the mean chemiluminescence image and radially integrated axial chemiluminescence intensity.

Results

In both theoretical and preliminary experimental studies performed in the previous period identified the parameters that govern the coherence between the globally integrated heat release rate and acoustic pressure fluctuations to be (1) the acoustic compactness described as κL_f which is the relative size of the flame to the acoustic wavelength, (2) the flame correlation length which describes the spatiotemporal statistics of the heat release, (3) the location of the observer, and iv) the flame geometry. Results can be interpreted in this context. Figure 6 shows the measured coherence and model predictions for Cases A1, A2, A3, and A5. These cases vary in flame length, which are mainly controlled by the equivalence ratio. The microphone is positioned at the coordinates $(x, y) = (0.2\,m, -0.2\,m)$. First, for Cases A1 and A5, excellent agreement between the measured results and model is observed. Consistent with results from the previous period, measured coherence trend towards unity at lower frequencies (i.e., the acoustically compact limit) as expected for a direct noise dominant system. Furthermore, the coherence roll-off is also extremely well predicted, validating the distributed monopole model which describes the acoustical noncompactness effect on coherence. For very rich conditions including Cases A2 and A3, while the roll-off trend is well predicted, some divergence from the model is observed, most notably the coherence at low frequencies asymptote to a value less than unity. It is believed that this is due to imperfect correlation between the unsteady heat release rate and chemiluminescence intensity associated with non-premixed flames.

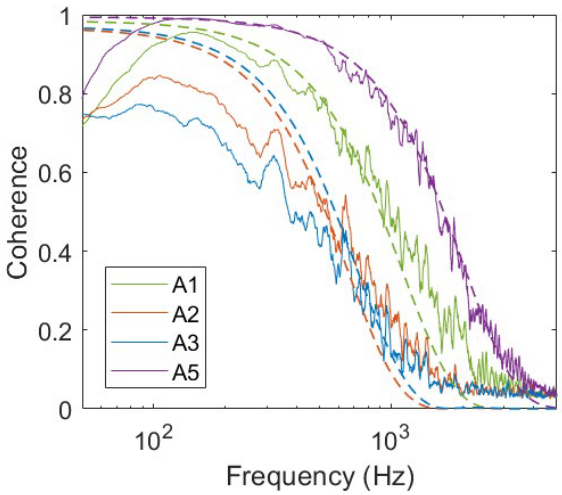

Figure 6. Measured coherence (solid) and model predictions (dashed) for Cases A1, A2, A3, and A5.

Since coherence roll-off is predicted to be a purely geometric phenomenon due to the distributed monopole nature of the source, it is possible to expect a universal form when normalized against the flame length. In Figure 7, an overlay of all test conditions is plotted. When normalized by the maximum coherence to account for the reduction in coherence associated with rich flames and plotted against the acoustic compactness factor κL_f, the plots collapse reasonably well, confirming predictions. Slight variance is expected as the axial heat release rate distribution for different operating conditions is not perfectly self-similar and thus not captured entirely within a single flame length. Comparing different definitions of the flame length, it was shown that $L_{f_{90}}$, which is defined as where 90% of the chemiluminescence intensity is observed, and $L_{f_{int}}$, which represents how spread out the distribution is and defined as $L_{f_{int}} = 3\int \left| z - L_{f_{max}} \right| Q dz / \int Q dz$, yields a good collapse. On the other hand, $L_{f_{max}}$ which is the location of the maximum axial heat release, performed

poorly, showing that it does not well represent the distribution of the axial heat release. Since some applications use $L_{f_{max}}$ or a similar definition for the flame length such as in $n-\tau$ type thermoacoustic instabilities, it is important to note how the flame length is defined for proper analysis.

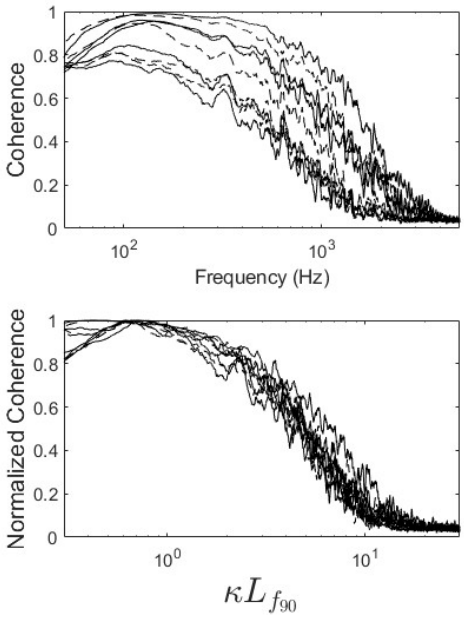

Figure 7. Overlay of coherence measured from all conditions (shown at top) and normalized coherence plotted against the acoustic compactness $\kappa L_{f_{90}}$ (shown at bottom).

As coherence roll-off is governed by the geometric relationship between the flame and observer, the observer location is also an important parameter of coherence. Previously, it was predicted that coherence is minimum along the primary dimension of the flame (i.e., for a long flame, the coherence is minimum along the centerline and vice versa). This is confirmed in Figure 8, where the normalized coherence for Case A3 is shown for different microphone locations. This effect is most prominent for long flames, hence Case A3 was chosen despite the necessity of normalization. As the microphone is moved to the side of the flame, coherence is increased, following model predictions. Deviations at the rightmost angle are due to the coherence roll off occurring at higher frequencies than what can be detected due to PMT measurement limitations. These results clearly show the role of observer location, especially angle, on coherence.

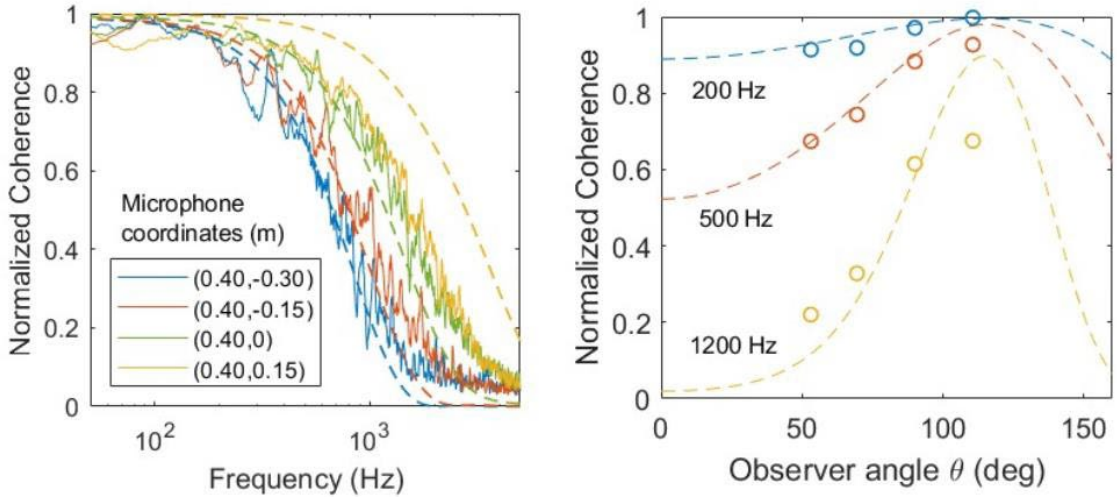

Figure 8. Normalized coherence measured at different microphone locations for Case A3 (left) and data plotted against the observer angle (right).

Having discussed the non-unity coherence at low frequencies for rich cases, further experiments were performed to investigate. Figure 9 shows the maximum coherence for Cases A6*, B6*, B7*, and B8* as a function of equivalence ratio. The phenomenon of a rapid decline of maximum coherence over a range of $\phi = 1.3 - 1.5$ followed by a plateau is observed across all cases tested. As this is not predicted by the distributed source model which agrees with other experimental results, it can be inferred that this phenomenon is not from the relationship between the unsteady heat release and acoustic pressure fluctuations. It is thought that the relationship between chemiluminescence intensity and heat release fluctuations are fundamentally different between premixed and non-premixed flames, and the coherence between the chemiluminescence and unsteady heat release is reduced as the non-premixed portion of the flame becomes significant. This also motivates a novel diagnostic method. As the coherence between the unsteady heat release rate and acoustic pressure is understood through this study, it is possible to gain insight into the relationship between chemiluminescence emissions and the heat release rate through coherence measurements. This is a point that deserves further study.

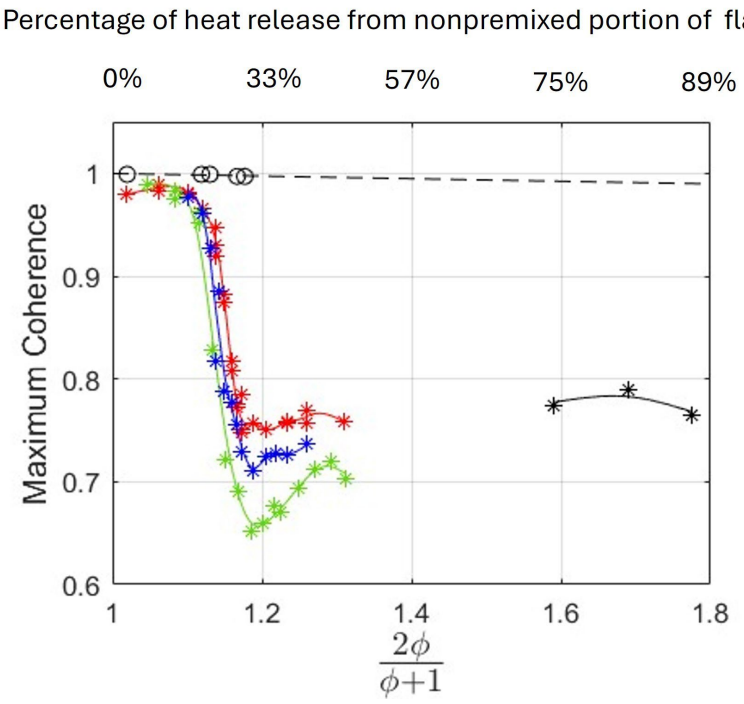

Figure 9. Maximum coherence across all frequencies, measured at various equivalence ratios. Red = A6*, $\frac{u'}{\bar{U}} \approx 8.5\%$, Blue = B6*, $\frac{u'}{\bar{U}} \approx 12.3\%$, Green = B7*, $\frac{u'}{\bar{U}} \approx 10.0\%$, Black = B8*, $\frac{u'}{\bar{U}} \approx 5.5\%$. Dashed line = extrapolated model prediction for maximum coherence.

Ducted configuration

The open flame experiment was equipped with a duct to verify new model predictions. The configuration is shown in Figure 10. In most practical applications, the flame is in an enclosed environment. Therefore, it is of interest to predict how coherence behaves in such a configuration. In the previous period, a two-dimensional (2D) model was developed to predict the effect of a duct based on the source image method. This model was also extended to a three-dimensional (3D) square duct. Figure 11 shows the coherence measured from microphone position 1 for the condition corresponding to Case A1. Model predictions, which were corrected to properly consider the increased speed of sound due to heating, show that the duct makes the coherence roll-off steeper, but also predicts a peak that appears after the initial decline. It is important to note that this peak is independent from the resonant duct modes and is caused by interference pattern-like effects from duct reflections. Indeed, the experimental results closely match such predictions, validating the image source model.

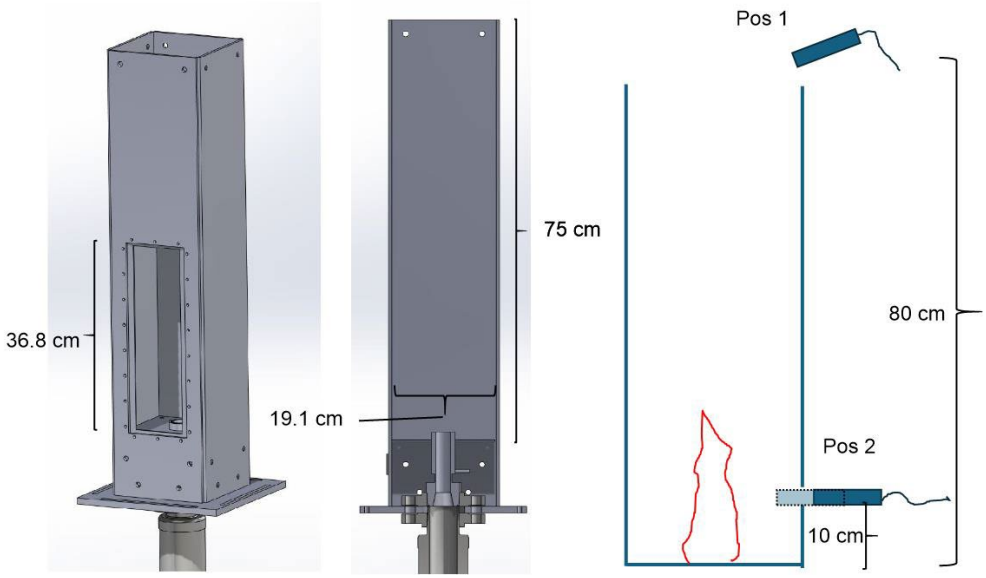

Figure 10. Ducted configuration of experiment.

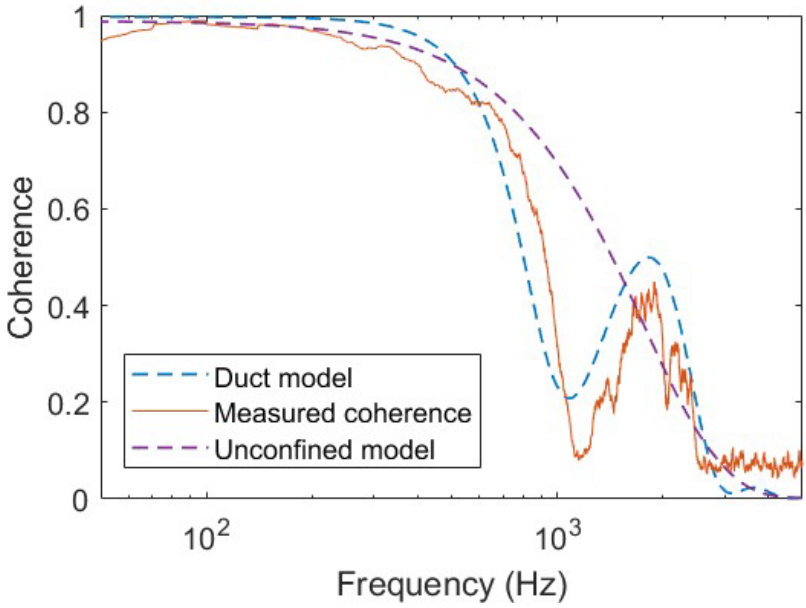

Figure 11. Coherence from microphone position 1, Case A1, for the ducted experiment.

Milestones

- Performed systematic study of coherence on open flame rig which was improved from the last period.
- Performed ducted studies on modified rig.

Major Accomplishments

- Made improvements on the rig and performed a systematic study on chemiluminescence-pressure coherence which successfully validated modeling efforts made in the previous period.

- Successfully implemented ducted configuration to open flame rig and validated model results.

Publications

Ha, S & Lieuwen, T. (2025). Direct combustion noise: Nearfield and non-compactness influences on pressure–heat release coherence, *Combustion and Flame,* Vol. 138, 113811.

Outreach Efforts

None.

Awards

None.

Student Involvement

Graduate student Sungyoung Ha is the lead experimentalist on the Georgia Tech rig.

Plans for Next Period

Dr. Ha graduated with his PhD Thesis in July 2025. Following his graduation, the work on this experiment will be continued in the next funding cycle.

Task 2 – GT Simulations

Georgia Institute of Technology

Objectives

Compressible multiphase reactive LES of the experimental rig are conducted under this sub-task to support the mechanistic understanding and ROM development for tonal noise. The computational configuration is a modification of the previous configuration used for the broadband noise program with a longer distance between the aft-end of the combustor and the choke point and a Variable Resonance Acoustic Screening Capability (VRASC) tube. The VRASC tube excites a tone, and this setup can then be used to evaluate strategies to mitigate the tone. The simulations are to be considered under three conditions. The baseline condition employs the same operating pressure, fuel-air-ratio (FAR), and air temperature (T3) as the previous match point from the broadband program. A higher-pressure condition is then simulated to match the RTRC experimental campaign for validation. Finally, a different combination of T3 and FAR is to be considered to evaluate the effect of modified mixing and combustion on the tone. Multiple time-dependent 3D snapshots are saved from LES and will be transferred to the RTRC and Georgia Tech ROM teams with sample post-processing scripts.

Research Approach

Solver Details

A fully compressible Eulerian finite-volume formulation for the gas phase and a Lagrangian formulation for the liquid phase are used in this study. An eddy-viscosity approach with a one-equation subgrid kinetic energy (k_{sgs}) model is used for the closure of gas-phase subgrid-scale fluxes. Because regions in which turbulence is not well established may exist in the plenum or outflow duct, the k_{sgs}-equation coefficients are set to constant values rather than being dynamically computed. Subgrid dispersion for spray particles is modeled with a stochastic separated flow model. Modeling of dense spray, corresponding compressible volume blockage effects, and breakup are also available, as we have previously shown, but these conditions are not considered herein; instead, a dilute injection of spray is considered. A well-established secondary breakup model based on Kelvin–Helmholtz instability is used.

The combustion is modeled via a finite-rate kinetics approach, by using a two-step, six-species mechanism for kerosene. Subgrid closure for turbulent combustion is provided by a simplified partially stirred reactor model, wherein the mixing time (τ_m) is computed locally by using k_{sgs}, and the chemical time (τ_c) is precomputed for the operating conditions from laminar premixed flame solutions under stoichiometric conditions. Further details about our modeling approach can be found in our recent works and are not repeated herein, for brevity.

The LES equations are solved at Georgia Tech using the in-house solver LESLIE. LESLIE is a well-established multi-block, structured, fully compressible finite-volume solver. A hybrid second-order central and third-order upwind method is used

for the gas-phase evolution. A fourth-order Runge–Kutta solver is used for solving the Lagrangian equations. For computational efficiency, instead of tracking individual Lagrangian particles, the particles are grouped together in "parcels," which are tracked in a Lagrangian manner. A particle-per-parcel value of 8 is used in this work, which has been shown to provide a good balance between accuracy and efficiency for gas-turbine combustor LES.

The current version of the Georgia Tech compressible solver contains three parts: (1) CFDPreProc, (2) LESLIE, and (3) CFDPostProc. CFDPreProc is a pre-processor that can perform functions such as creating a grid and setting boundary conditions. LESLIE is a core compressible solver that conducts multi-phase reactive LES. The latest LESLIE code (improved during the Year 2 efforts) outputs 3D snapshots of conservative variables that are directly solved for in our compressible framework, including the density, momentum, total energy, and partial densities. Primitive variables remain required for the computation of noise-related quantities; therefore, CFDPostProc computational fluid dynamics (CFD) post-processing software is used to read the conservative variable-based 3D snapshots and compute additional primitive quantities. This code is provided to the RTRC and Georgia Tech ROM teams along with the 3D snapshots. The conservative variables form an exclusive and exhaustive set of variables; therefore, all other quantities can be computed from this set.

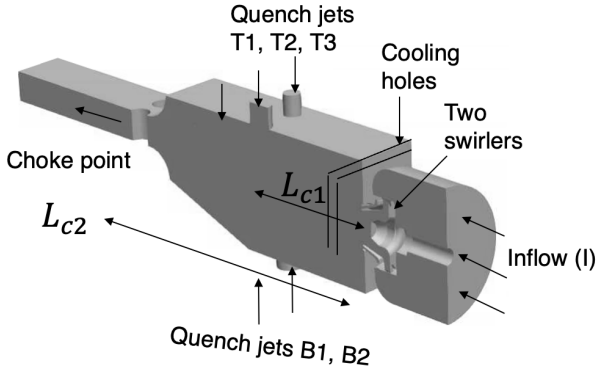

Computational configuration for LES, Original configuration

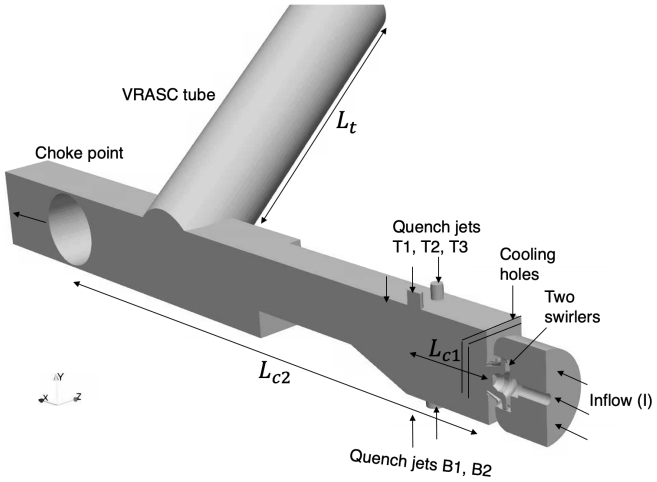

Computational configuration for LES, New configuration

Figure 12. Computational configurations for LES. Original configuration used for broadband program (shown in the top). New configuration with Variable Resonance Acoustic Screening Capability (VRASC) tube for tonal noise studies (shown in the bottom). Key features and corresponding boundary conditions are shown.

Computational Configuration

The computational configurations are shown in Figure 12. Both the original configuration used for the broadband program and the new configuration with the VRASC tube are shown. The flow from the inlet plenum enters the combustion chamber via two concentric swirlers (one axial and one radial). After the reaction zone, three quench jets on the top, and two on the bottom, are available to reduce the temperature. In addition, multiple small cooling holes are present on the bulkhead (or faceplate) to decrease the wall temperature. The flow exits the outflow duct through either the choked jail bars (original configuration) or a cylindrical choke point that is at a much longer distance after the combustor and with the VRASC tube in between (new configuration). The region between the bulkhead and the quench jets is where most of the heat release occurs and its length is denoted as L_{c1}. This part of the geometry is the same between the original and the new configurations. The distance between the bulkhead and the choke point is denoted as L_{c2}. It is approximately 2.5 times longer for the new configuration compared to the original configuration. The length of the VRASC tube is fixed and denoted here as L_t. This matches the reference value from the experiments.

All gas-phase inlet boundary conditions (ahead of the inlet plenum [I] and dilution holes [T1, T2, T3, B1, and B2]) specify a constant mass flow rate based on experimental inputs and are modeled with a characteristic Navier–Stokes boundary condition. The mass flow rate for the main inflow (I) is set as 25.0% of the total air flow rate. The total mass flow rate through the top (T1, T2, and T3) or bottom (B1 and B2) quench jet holes is 31.2% of the total. The cooling holes on the bulkhead are not resolved; therefore, they are modeled as a porous boundary condition. The mass flow rate specified through these cooling holes is 12.5% of the total. The incoming air is at T3=673.3K. The flow at the computational outflow (O) is always supersonic and extrapolation boundary conditions are used for it. No waves are expected to travel upstream into the combustor chamber from this region, because the flow is choked.

The fuel is injected as Lagrangian spray droplets in a stochastic manner with two concentric injectors. The total fuel mass flow rate is chosen to impose a global FAR of 0.025 and a global equivalence ratio of 0.37. The fuel mass flow rate through the primary injector is 25.8% of the total and through the secondary injector is 74.2% of the total. In the absence of any experimental measurements for this injector, a log-normal size distribution with Sauter mean diameter 55 μm is injected. A secondary breakup model based on Kelvin–Helmholtz instability is used that breaks the injected droplets into smaller droplets through a physics-based approach on its own. These modeling choices are like the previous gas-turbine LES. The primary injector is modeled as a solid cone injector with a 60° angle; the secondary injector surrounds the primary injector and is modeled as a hollow cone injector with 90° and 120° inner and outer angles, respectively. The injection temperature of the liquid fuel is 330K, and the velocities are set to 25 m/s. This dilute injection occurs 1 mm downstream of the actual injector plate. This injection procedure is empirical but could be improved in the future, based on experimental insights.

The multi-block structured grids for both the original and new configuration have approximately 6.8 million cells and grid clustering is applied to the near region of the shear flow from the swirler and exit plenum. For handling geometrical complexities, up to eight multi-block structure grids are generated with hanging nodes, which are stitched together via an interpolation technique of the same order as the numerical scheme used. Shear layers are resolved with 10–15 points across, and the swirlers have 10 or more points along their span, in agreement with previous LES. The LES solver is parallelized, and the simulations are run on 512 cores. The flow-through time of the combustor is estimated are $t_{flow} = L_{c1}/U_{bulk}$, where U_{bulk} is an approximate bulk flow velocity in the combustor. Since the combustor configuration and the bulk flow velocities are the same across all tests, a reference frequency for normalization is defined as $f_0 = 1/t_{flow}$. For all simulations, the initial transients are neglected for at least the first two flow-through times or until the chamber pressure and volume-integrated heat release rate (HRR) stabilize. The statistics are then collected over at least ten additional flow-through times. A simulation for a single flow-through time uses 11,605 central processing unit (CPU) hours on Georgia Tech's supercomputing cluster (Partnership for an Advanced Computing Environment-Phoenix) with Intel® Ivy-bridge i7 processors.

The comparison here considers three operating conditions. These are listed in Table 2. Case-0 refers to the match point from the previous broadband program with the old configuration that used jail bar for flow choking. The LES results at these conditions were validated against the experimental measurements in the past. Case-1 retains the same operating pressure, FAR, and T3 as Case-0, but uses the new geometry with the VRASC tube. Case-2 keeps the T3, FAR, and geometry the same as Case-1 but raises the chamber pressure by 1.4 times to match the RTRC experiments. The increased chamber pressure is achieved by keeping the same geometry and choking area but proportionately increasing all the mass

® Intel is a registered trademark of Intel Corporation, Santa Clara, California.

flow rates (fuel and air). An additional test, Case-3, is also being considered with modified FAR and T3. Further details and results for this will be provided in the next reporting period. All simulations are run with the same solver and model choices. Throughout this report, the chamber pressure of Case-0 is referred to as the reference pressure p_0 and is used to normalize all the results.

Table 2. List of simulated operating conditions.

Case	Normalized Pressure	FAR, T3	Geometry
Case-0 (Match point)	1.0	Ref. values	Jail bar choking
Case-1	1.0	Ref. values	VRASC tube
Case-2	1.4	Ref. values	VRASC tube

The LES captures unsteady turbulent combustion. The predicted temperature field at a representative instance is shown in Figure 13 for reference. As expected for a typical swirl-stabilized combustor, it shows a wrinkled flame structure with hot center and corner recirculation zones. The flow cools down upon mixing with the quench jets. Further quantification of this process is provided in the next sections. For demonstrating the sufficiency of the LES grid, the turbulent kinetic energy (TKE) is computed at a representative point in the shear layer, as shown in Figure 13, and the results capture the inertial subrange over more than a decade. This result has been confirmed at other points within the combustor (i.e., cooling jets, swirling shear layer, etc.), but these data are not shown herein, for brevity.

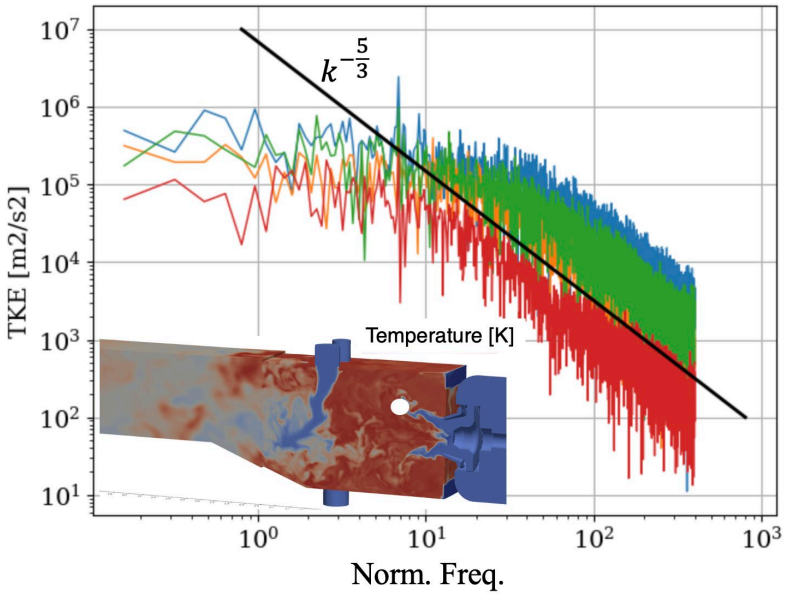

Figure 13. Turbulence and flame interaction in combustor: Predicted unsteady temperature field at a representative instance is shown in the sub-figure. Turbulent kinetic energy (TKE) spectrum at a representative point in the shear layer shows at least a decade of inertial range turbulence.

Pressure Dynamics

A key metrics for LES validation and combustion noise analysis is the pressure spectra or the sound pressure level (SPL) at a fixed probe location. The previous results for Case-0 matched the Georgia Tech experimental measurements in terms of the SPL broadband decay rate and peak locations and magnitude. For a probe located on the ramp after the quench jets, and the LES results predicted the decay of pressure spectra between f/f_0 4.8 and 16 and peaks near f/f_0 6.4 and 20.8. The peak at f/f_0=20.8 was shown to correspond to the first longitudinal acoustic mode. Further details on this validation exercise can be found in the previous reports and are not repeated here.

The current comparison between the different cases is for a probe placed on the bulkhead. The results for Case-0, Case-1, and Case-2 are compared in Figure 14. Unlike Case-0, which showed a broadband spectrum, the addition of the VRASC tube in Case-1 and Case-2 clearly enhances a much stronger tonal behavior. Two frequencies of interest are f/f_0=6.8 and 18.8. The latter is the strongest tone for Case-1 (reference pressure), and former is the strongest tone for Case-2 (higher pressure). Both tones are present in both configurations but with different relative strengths.

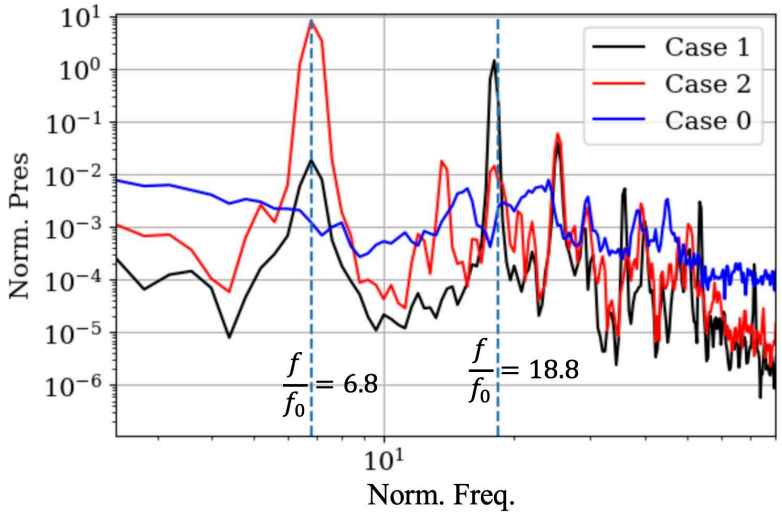

Figure 14. Pressure spectra from LES at a point on the bulkhead. Some notable frequencies are shown as vertical lines.

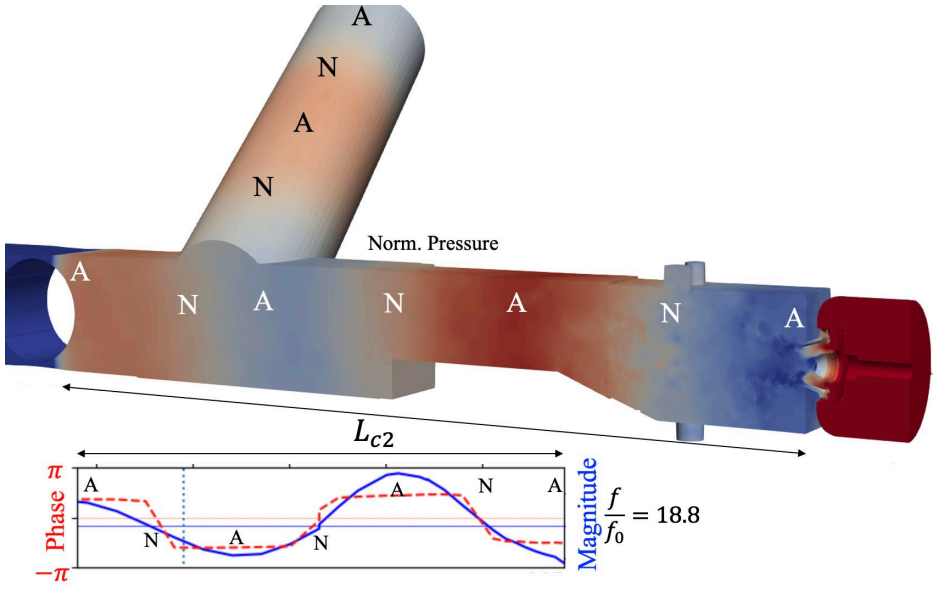

Figure 15. Case 1, Instantaneous pressure contours (shown in the top), phase and magnitude of pressure signal along the center (shown in the bottom). Corresponding pressure nodes (N) and anti-nodes (A) are also noted.

To further evaluate the nature of these tones, the pressure dynamics in the system is further analyzed through a phase-magnitude analysis. Corresponding results for Case-1 and Case-2 are shown in Figure 15 and Figure 16 respectively. 3D contours of instantaneous normalized pressure are also shown for reference. Case-1 showed the strongest tone at

f/f_0=18.8 and therefore the phase-magnitude analysis for Case-1 is at this frequency. The results confirm a longitudinal acoustic mode that is also coupled with the VRASC tube, and which shows the phase switching at the nodes and zero or largest magnitude at the nodes or the anti-nodes, respectively. The identified pressure node and anti-nodes are also noted in the 3D picture for reference.

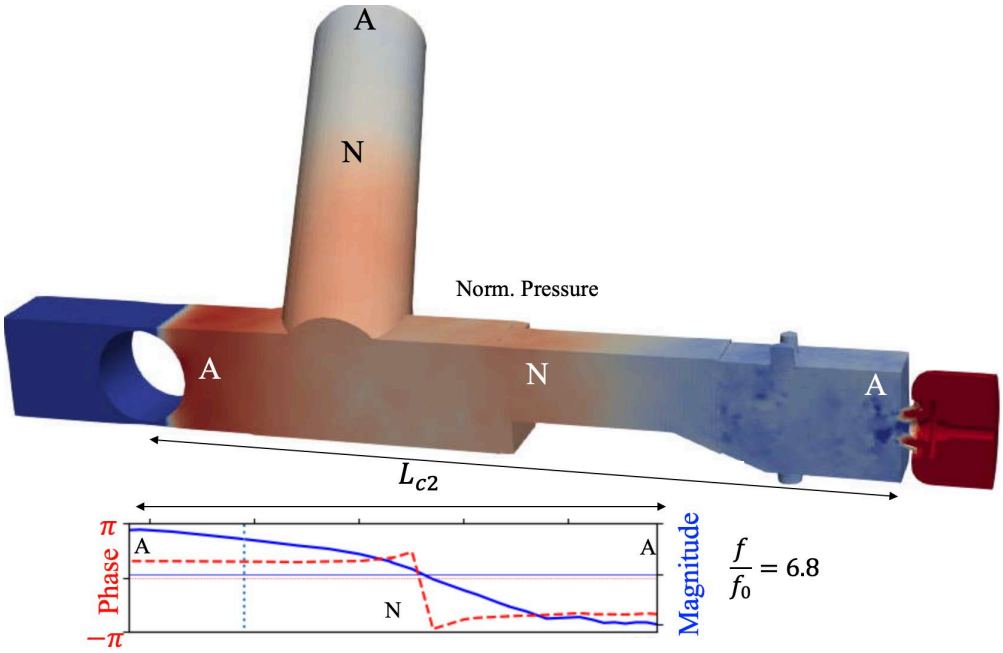

Figure 16. Case 2, Instantaneous pressure contours (shown in the top) and phase and magnitude of pressure signal along the center axis (shown in the bottom). Corresponding pressure nodes (N) and anti-nodes (A) are also noted.

A similar analysis for case-2 is also conducted at f/f_0=6.8 as shown in Figure 16. This is a lower order acoustic mode with only two nodes in the entire configuration, but it has a much stronger magnitude compared to Case-1 as confirmed from the pressure spectra. The phase-magnitude analysis is also conducted at other frequencies for both cases, and the results show that the 6.8 and 18.8 modes are present in both Case-1 and Case-2 but only one of them is activated depending on the operating pressure. The reasons for this are discussed in the next section. It is also noted that the mode shape and frequency for Case-2 is qualitatively consistent with the experimental observations from RTRC, but a one-to-one comparison is not conducted yet. This will be considered in the future as experimental data become accessible.

Heat Release Rate Dynamics

Unsteady HRR data are crucial for mechanistic understanding of combustion tones or ROM development. The overall burning is expected to occur in the swirling shear layers as the incoming droplets disperse, vaporize, and burn while interacting with a hot recirculation zone. In the past, for Case-0, the time-averaged and line-of-sight heat release rate from LES was compared against OH* chemiluminescence data from the Georgia Tech experiments for validation. These results showed a reasonable match in terms of the flame structure. The new results for Case-1 and Case-2 are shown in Figure 17. A qualitatively similar flame shape is observed for both the new configurations although there are significant quantitative differences between Case-1 and Case-2. The flame in Case-2 (higher pressure) is much longer along the combustor axis while the transverse extent is the same. A comparison with experimental measurements will be considered in the future as data become available. As shown later, the combustion in both Case-1 and Case-2 is actively coupled with a longitudinal acoustic mode but at different frequencies and this is the cause of the observed differences.

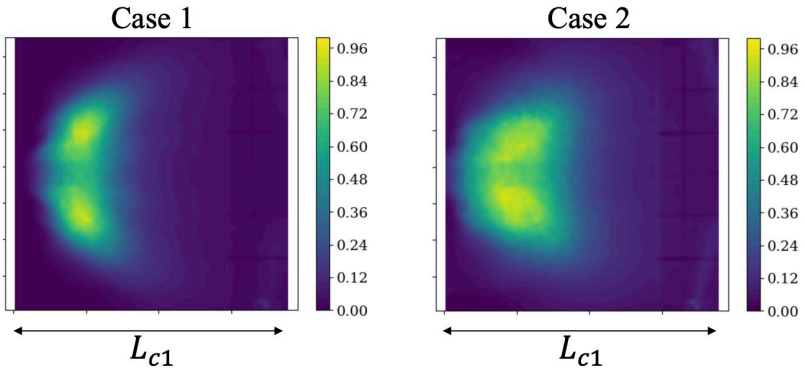

Figure 17. Case 1 (left) and Case 2 (right) time-averaged and line-of-sight averaged heat release rate contours.

The time-averaged view of the heat release does not provide any information about the dynamical features of the flame, which is necessary for understanding combustion noise mechanisms. Power spectral density (PSD) of volume-averaged HRR is shown in Figure **18**. These results show that HRR dynamics is coupled with the previously discussed pressure dynamics. Both Case-1 and Case-2 show strong peaks in the HRR spectra at f/f_0=18.8 and 6.8, respectively. Unlike the pressure, where both f/f_0=18.8 and 6.8 were present for both cases with different magnitudes, the HRR spectra only shows a frequency corresponding to the most dominant mode. This suggests that even though both the acoustic modes are present in the combustor, only one of them is activated and coupled with heat release and combustion. The HRR spectra does show a presence of harmonics of f/f_0=18.8 of 6.8 near approximately f/f_0=37.6 and 17.6 for Case-1 and Case-2, respectively.

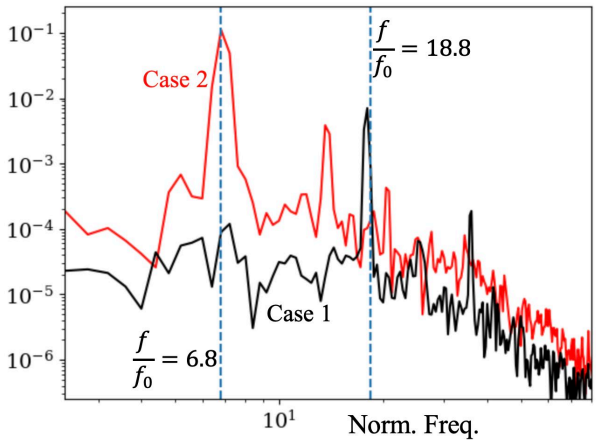

Figure 18. Spectra of volume averaged normalized heat release rate (HRR). Notable frequencies are shown as vertical lines.

The dynamical flame structures are further analyzed using a Proper Orthogonal Decomposition (POD) analysis of the 3D heat release rate. The first four most energetic modes and spectra of their mode coefficients are shown in Figure 19. Additional modes with a lower energy are also analyzed but not shown here. The spectral behavior of the first two mode coefficients clearly shows the presence of the activated 16.8 (for Case-1) and 8.8 (Case-2) modes and their harmonics. The shapes of both these modes show primarily a longitudinal variation suggesting a coupling with the longitudinal acoustic waves. The spectra of higher order mode coefficients show a nearly broadband behavior. Furthermore, even though there are qualitative similarities between the mode shapes of Case-1 and Case-2, clear quantitative differences are noticeable. This may suggest that a POD based reduced order model developed for Case-1 may not be applicable to Case-2 which

operates at a higher pressure, activates a different thermoacoustic mode, and results in quantitatively different POD modes.

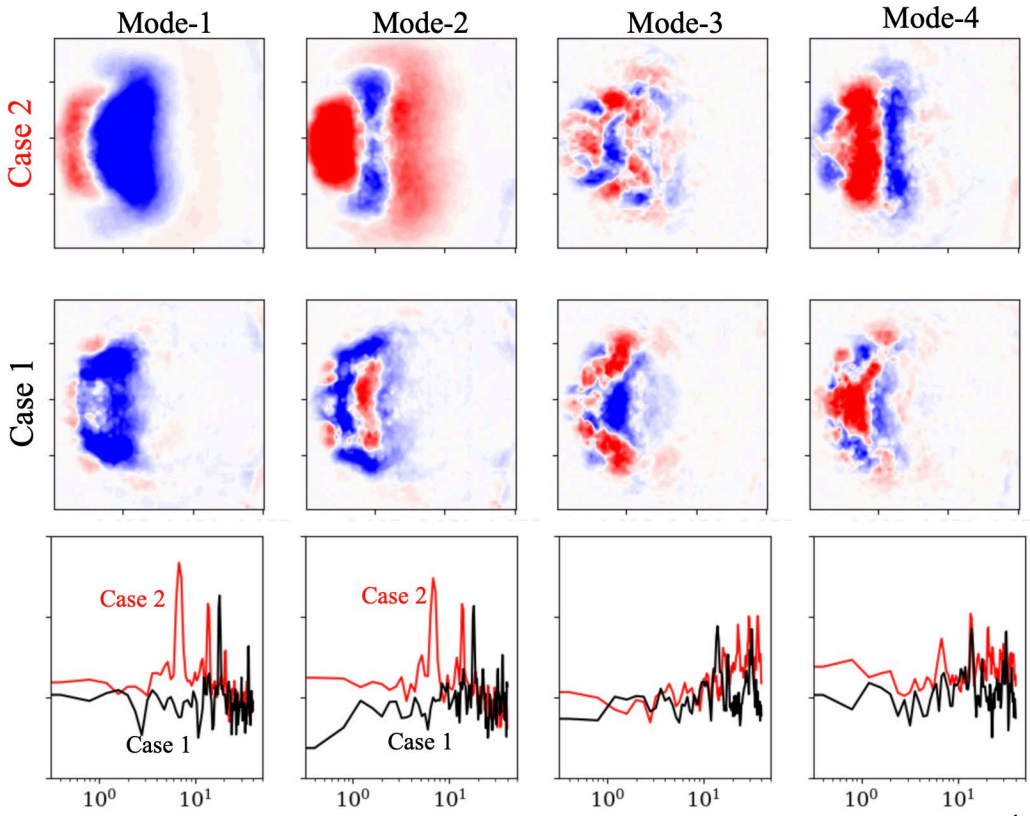

Figure 19. Proper Orthogonal Decompositions of normalized HRR: The shapes of first four most energetic modes are shown for Case-1 (top row) and Case-2 (middle row). The POD analysis is conducted using three-dimensional snapshots, but the mode shapes shown here are spanwise averaged to highlight the differences. The spectral signature of mode coefficients is also shown for Case-1 and Case-2 (bottom row).

A reliable way of identifying thermoacoustic instabilities is the Rayleigh Integral Criterion (RI). This is defined as the volume integral $\int_V p'q'$, where p' is the pressure perturbation and q' is the heat release perturbation. This criterion evaluates if the pressure and the heat release rate oscillations are in-phase or out-of-phase. The in-phase oscillations result in RI>0 and they would suggest a growing or limit-cycle thermoacoustic instability. On the other hand, RI<0 would suggest a damping thermoacoustic instability. The PSD of the RI identifies the frequencies where this coupling is happening, and these results are shown in Figure 20 for both Case-1 and Case-2. The results show that the thermoacoustic coupling is in general stronger for the higher-pressure configuration Case-2 and occurs at f/f_0 =8.8. On the other hand, the coupling for Case-1 occurs at f/f_0 =18.8. These results confirm that f/f_0 =8.8 (for Case-2) and f/f_0 =16.8 (for Case-1) are thermoacoustic instabilities operating in a limit-cycle. All the other frequency peaks of the RI in Figure 20 correspond to either harmonics or sub-harmonics of these dominant frequencies.

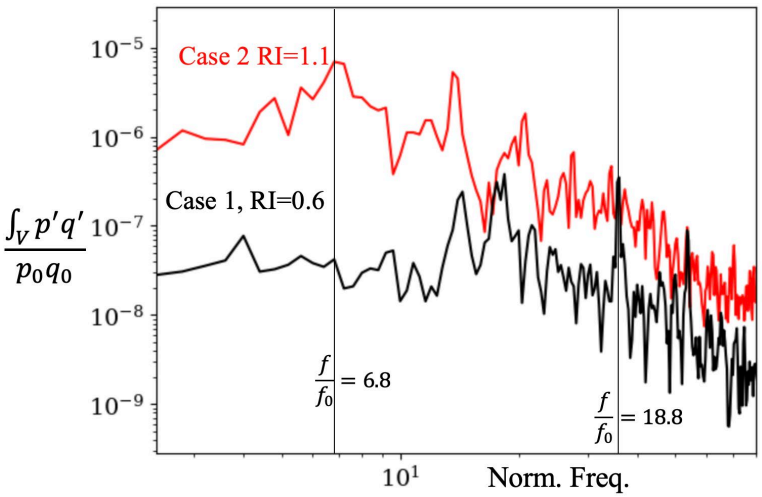

Figure 20. Power spectral density of normalized Rayleigh Integral Criterion (RI) is compared between Case-1 and Case-2. The time-averaged values of RI are noted for both cases. Some notable frequencies are shown as vertical lines.

Data Output and Transfer

The simulations output 3D snapshots of conservative variables. The output frequency of these outputs is f/f_0 =80 and at least 1,000 such snapshots are output for each case over the span of at least 10 flow-through times. The snapshots are collected only after the initial transients for the first two flow-through times have been neglected. A single 3D snapshot is approximately 1 GB in size. The CFDPostProc software and sample post-processing scripts can (a) compute primitive quantities, such as pressure, temperature, density, and reaction rates, (b) compute derivatives, (c) compute time-averaged quantities, and (d) interpolate data onto another rectangular grid from these files.

In addition to the 3D gas-phase snapshots, the Lagrangian data of the parcel are saved at the same frequency and are available for computing the spray droplet statistics. A post-processing script that translates the Lagrangian quantities onto a Eulerian grid via filtering is also available and provided to other teams. A single droplet snapshot is approximately 50 MB in size.

Because the 3D gas-phase snapshots are large, they could not be collected at higher frequencies. However, the simulation collects high-frequency data at f/f_0 =800 for approximately 200 probe points distributed throughout the computational domain. These points are uniformly placed along the *x*/*y*/*z* directions within the combustor, through the nozzle, and within the exit plenum. These data can be used for accurately computing the frequency characteristics of the system.

Finally, although time-averaged statistics (i.e., mean, root mean square [RMS]) can be computed by using the output 3D snapshots, fine-grained time averaging is also conducted within the code, and the mean and RMS primitive quantities are output for the entire 3D domain. These quantities include primitive variables, such as velocity, temperature, pressure, density, species mass fractions, and reaction rates. The size of a single time-averaged file is ~4 GB.

Milestones

- Conducted LES of the new experimental configuration with a VRASC tube for tonal noise predictions.
- The results show a clear presence of limit-cycle thermoacoustic instability. The frequency depends on the operating pressure and is qualitatively consistent with experimental observations.
- Multiple time-dependent 3D snapshots are collected for each operating condition to be provided to the ROM development teams with relevant post-processing scripts.

Major Accomplishments

Grid modifications and additional LES were conducted in Year-5 to study tonal combustion noise. The predictions show a limit-cycle combustion instability a qualitatively consistent behavior with the experiments. The oscillation frequency depends on the operating pressure.

Publications

Kastenberg, L. M., Panchal, A., & Menon, S. (2025). Direct and Indirect Combustion Noise Prediction in a Rich-Quench-Lean Combustor Using a Large Eddy Simulation. *AIAA SciTech Forum*, AIAA 2025-2489.

Outreach Efforts

None.

Awards

None.

Student Involvement

- Graduate student Leo Kastenberg graduated with a master's degree with thesis in August 2025. He worked on detailed validation of the LES results using POD and developing post-processing scripts for 3D snapshots, entropy processing, and direct and indirect noise identification.
- Graduate student Sathvik Gujjati, who is pursuing a master's degree with thesis, is currently working on grid refinement studies and will conduct LES at additional conditions in the future.

Plans for Next Period

- Consider a detailed validation of the new LES predictions against the experimental measurements if data become available. The comparison will use pressure probe and Chemiluminescence data.
- Conduct additional LES with modified FAR and T3 to study the effect of mixing and combustion on tonal noise. These conditions will be chosen consistently with the experimental campaign.
- Transfer all results and 3D snapshots to the ROM development team with relevant post-processing scripts.

Task 3 – GT Reduced-Order Modeling

Georgia Institute of Technology

Objective

The overarching objective of this task is to create quick-action ROMs to accurately predict various aspects of noise generation mechanisms that are then collectively fed into a design tool for noise prediction. The specific objective of the Georgia Tech ROM task focuses on the head-end physics in the architecture, namely the flow and spray dynamics, flame dynamics, and generation of entropy disturbances by the flame. The spray/flow dynamics feed into the flame dynamics, thus causing direct combustion noise. The flame dynamics also results in entropy disturbances, which in turn lead to indirect combustion noise at the nozzle. The flame response modeling and the model for the generation of entropy disturbances are provided as inputs to the post-combustion models that will be developed by RTRC. Depending on the prediction results obtained from the RTRC models, these head-end models will be iteratively refined.

Research Approach

In this reporting period, our team focused on tasks pertaining to hydrodynamics, coherence and entropy generation. Each of these tasks are detailed in their respective subsections below.

Hydrodynamics Modeling

In this reporting period, the hydrodynamics framework was extended to perform validation strategies for the swirling jet global stability analysis. Swirling flows usually result in unsteady hydrodynamic structures that can couple with acoustics. Thus, modeling and predicting the hydrodynamic structures arising from swirling jets is a key challenge, particularly in the presence of combustion, because these structures can interact with and perturb the flame. As discussed in the previous yearly report, global hydrodynamic stability predicts stable and unstable vortical modes of a time-averaged flow field. However, the instantaneous LES time snapshots of velocity fields can be used to detect coherent structures of the spatio-temporal flow field using data-driven modal decompositions.

For this study, space-only POD was used to separate the instantaneous velocity fields $u'(\boldsymbol{x},t)$ into deterministic spatial functions $\boldsymbol{\Phi_k}(\boldsymbol{x})$ and their modulating time coefficients $a_k(t)$:

$$u'(x,t) = u(x,t) - \bar{u}(x) = \sum_{k=1}^{\infty} a_k(t)\Phi_k(x) \quad \text{(Eq. 1)}$$

The mean-subtracted, planar velocity fluctuations at each time snapshot are then arranged as a column vectors and stacked side-by-side, forming the snapshot data matrix with m spatial points and n time snapshots.

$$U = \begin{bmatrix} u'(x_1,t_1) & u'(x_1,t_2) & \cdots & u'(x_1,t_n) \\ u'(x_2,t_1) & u'(x_2,t_2) & \cdots & u'(x_2,t_n) \\ \vdots & \vdots & \ddots & \vdots \\ u'(x_m,t_1) & u'(x_m,t_2) & \cdots & u'(x_m,t_n) \end{bmatrix} \quad \text{(Eq. 2)}$$

An economy-sized singular value decomposition (SVD) or $\mathbf{U} = \Phi\Sigma\Psi^T$ provides the POD modes and coefficients of the unsteady spatio-temporal data. Snapshot POD orders the modes according to their turbulent kinetic energy (TKE) when the input data consist of constant-density velocity fluctuations. The contribution of the k^{th} mode to total TKE is given by the σ_k or the diagonal elements of the matrix Σ:

$$E_k = \frac{\sigma_k^2}{\mathrm{Tr}(\Sigma)} = \frac{\sigma_k^2}{\sum_{k=1}^{min(m,n)} \sigma_k^2} \quad \text{(Eq. 3)}$$

Instantaneous $n = 1{,}473$ time snapshots with a time step of $\Delta t = 0.1$ ms or sampling frequency of $f_s = 10$ kHz are interpolated on a center line slice with 128×128 spatial grid points. Figure 21 displays an instantaneous axial velocity snapshot of this sliced dataset on the 128×128 spatial mesh.

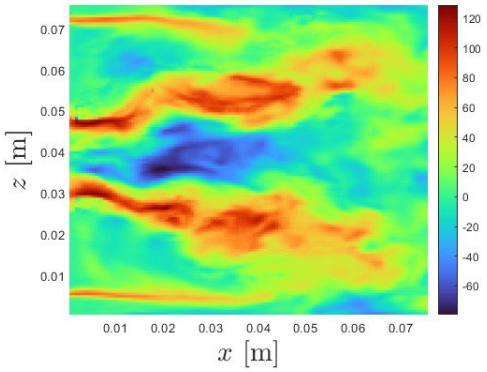

Figure 21. Instantaneous snapshot of axial velocity along center-line plane.

After application of POD to the instantaneous data, Figure 22 shows the spectrum of leading POD modes and their respective contribution to the total TKE. POD mode 1 accounts for approximately 10 percent of total turbulent kinetic energy present in the planar velocity flow field. Modes 2 and 3 each contain approximately half of the energy of the leading mode, while the energy in subsequent modes slowly decreases. The cumulative percent contribution to TKE shows the smooth and slow convergence of the POD spectrum, which is typical for turbulent shear flows.

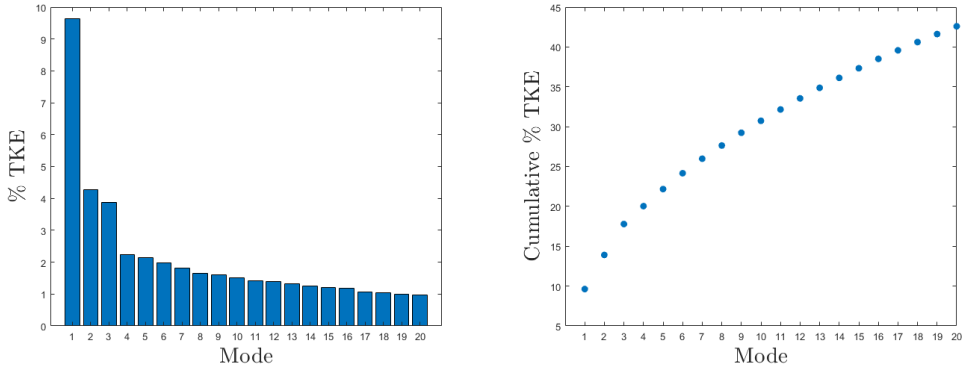

Figure 22. Individual and cumulative TKE distributions for leading POD modes.

Figure 23 shows the leading 12 POD modes, accounting for approximately 35% of TKE. The spatial mode shapes are displayed using the out of plane vorticity computed from the planar velocities of the POD modes. Planar velocity streamlines are overlaid to indicate vortex shedding structures in the domain. The highly energetic Mode 1 represents a shear-layer flapping mode, while Modes 2, 3 and 4 display distinct large length-scale out-of-plane vortical structures. These structures indicate sinuous modes, in which shear layer vorticity coalesces anti-symmetrically. Modes 5-8 contain a mix of both small length-scale and large length-scale vortex structures but display varicose behavior, in which shear layer vorticity coalesces symmetrically about the centerline. Lastly, Modes 9-12 are dominated by several smaller scale shear layer vortices shedding in the nozzle near-field with an anti-symmetric sinuous shedding fashion.

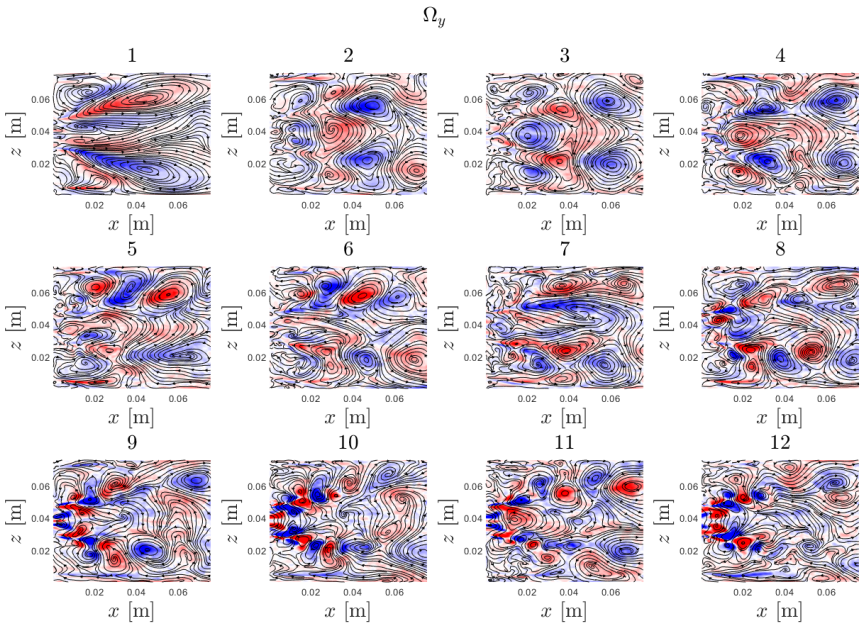

Figure 23. Leading center-line planar vorticity of leading POD mode shapes.

To understand the behavior of the modes in frequency space, window-averaged Welch's method is used to compute an estimate of the PSD by dividing the time coefficients of the leading POD modes into overlapping segments. Figure 24 displays the PSD amplitude of the leading modes in frequency space. Modes 2 and 3 display a broadband peak around 0.6

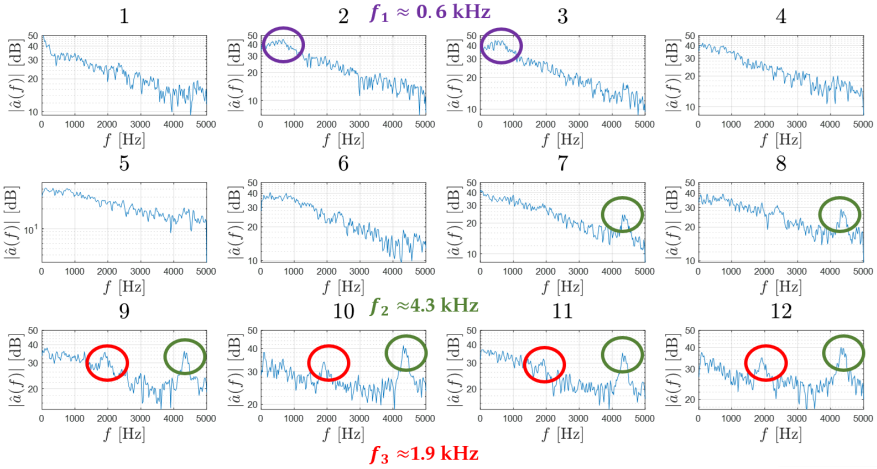

Figure 24. Power spectral density amplitude of time coefficients of leading POD modes.

The results from snapshot POD indicate that the high-energy POD modes capture inner and outer shear layer structures from the instantaneous data. Furthermore, there exists a large length-scale, lower-temporal frequency pattern dominating the downstream region, while a shorter length-scale, higher-frequency pattern is evident in the near-nozzle region. However, many of these features appear to be split over several POD modes as some of the POD modes appear to capture a noticeable mixture of these different vortex patterns. This is evident by both the spatial patterns and the multi-peak PSD spectra. A secondary validation study using advanced modal decomposition techniques such as spectral proper orthogonal decomposition and dynamic mode decomposition can be conducted to better identify spatially correlated features with different temporal behavior.

Modeling *p'-q'* Correlation/Coherence

The objective of this task is to study the correlation between the HRR measured by chemiluminescence and the generated noise, specifically direct noise. Through modeling and comparison with experimental data, it is possible to understand the governing physics behind coherence and extend results to any hypothetical flame configuration. Throughout the last several periods, an analytical model was successfully developed to study the effects of acoustic noncompactness and nearfield effects on the *p'-q'* coherence of an open flame. It demonstrated how these effects could act to lower coherence even in the case of a direct noise dominant system. Recent results in the GT Experimental task verified these findings, enabling predictions for future configurations.

In the previous period, the open flame model was extended to a 2D ducted configuration to study the effect of confinement. In this period, this 2D model was expanded to a 3D square duct for comparison with experimental data. To restate the approach, in the previous analytical model has shown that the parameters that govern coherence were identified as (1) the normalized flame correlation length $\frac{\Lambda}{a}$, (2) the "compactness factor" $\frac{a}{\lambda}$, (3) the distance of the observer $\frac{R}{a}$, and (4) the flame aspect ratio $\frac{L_f}{a}$. Starting from the linear wave equation:

$$\frac{\partial^2 p'(x,t)}{\partial t^2} - c_u^2 \nabla \cdot \left(\frac{\rho_u}{\rho_0} \nabla p'(x,t)\right) = (\gamma - 1)\frac{\partial q'(x,t)}{\partial t} \qquad \text{(Eq. 4)}$$

The Fourier transformed solution can be written as:

$$p'(x_0,\omega) = \frac{-i\omega(\gamma-1)}{4\pi c_u^2} \oint q'(x_s,t) G(x_s,x_0,\omega) dS \qquad \text{(Eq. 5)}$$

where $\boldsymbol{G}(x_s,\ x_0)$ is the Green's function for a source at x_s and the observer at x_0. From here on the Fourier transformed variables are considered. In the free field, it is well known that Green's function takes the form:

$$G(x_s, x_0, \omega) = \begin{cases} \frac{e^{ik|x_s - x_0|}}{|x_s - x_0|} & \text{3D freefield} \\ \frac{i}{4} H_0^{(1)}\left(\frac{2\pi|x_s - x_0|}{\lambda}\right) & \text{2D freefield} \end{cases} \quad \text{(Eq. 6)}$$

where $H_0^{(1)}$ is the Hankel function of the first kind of the zeroth order. Then, it is possible to write the auto spectra of the acoustic pressure G_{pp}, the global HRR G_{QQ}, and the cross spectra G_{Qp} as:

$$G_{QQ} = \iint q'(x_{s_1})\, q'^{*}(x_{s_2}) ds_1 ds_2 \quad \text{(Eq. 7)}$$

$$G_{pp} = \frac{\omega^2(\gamma-1)^2}{16\pi^2 c_u^4} \iint q'(x_{s_1})\, q'^{*}(x_{s_2}) G(x_{s_1}, x_0) G^{*}(x_{s_2}, x_0) ds_1 ds_2 \quad \text{(Eq. 8)}$$

$$G_{Qp} = \frac{i\omega(\gamma-1)}{4\pi c_u^2} \iint q'(x_{s_1})\, q'^{*}(x_{s_2}) G^{*}(x_{s_2}, x_0) ds_1 ds_2 \quad \text{(Eq. 9)}$$

Previously, the Green's function was developed for a 2D duct using the method of image sources. The same principle applies to a 3D square duct, where the image source now considers reflections from all surroundings as shown in Figure 25. The resulting Green's function is expressed as:

$$G(x_0, y) = \sum_{n=0}^{N} \sum_{n_x=0}^{n} \sum_{n_y=0}^{n-n_x} \left[\frac{exp\left(\frac{-2\pi i|y^n - x_0|}{\lambda}\right)}{|y^n - x_0|} + \frac{exp\left(\frac{-2\pi i|y^{*n} - x_0|}{\lambda}\right)}{|y^{*n} - x_0|} \right] \quad \text{(Eq. 10)}$$

where if $y^n = (y_x^n, y_y^n, y_z)$, $y^{*n} = (y_x^n, y_y^n, -y_z)$,

$$y_x^n = \begin{cases} \pm 2n_x r - y_x, n_x\ is\ odd \\ \pm 2n_x r + y_x, n_x\ is\ even \end{cases}$$
$$y_y^n = \begin{cases} \pm 2n_y r - y_y, n_x\ is\ odd \\ \pm 2n_y r + y_y, n_x\ is\ even \end{cases}.$$

Results and comparison with experimental results are discussed in the GT experimental task section.

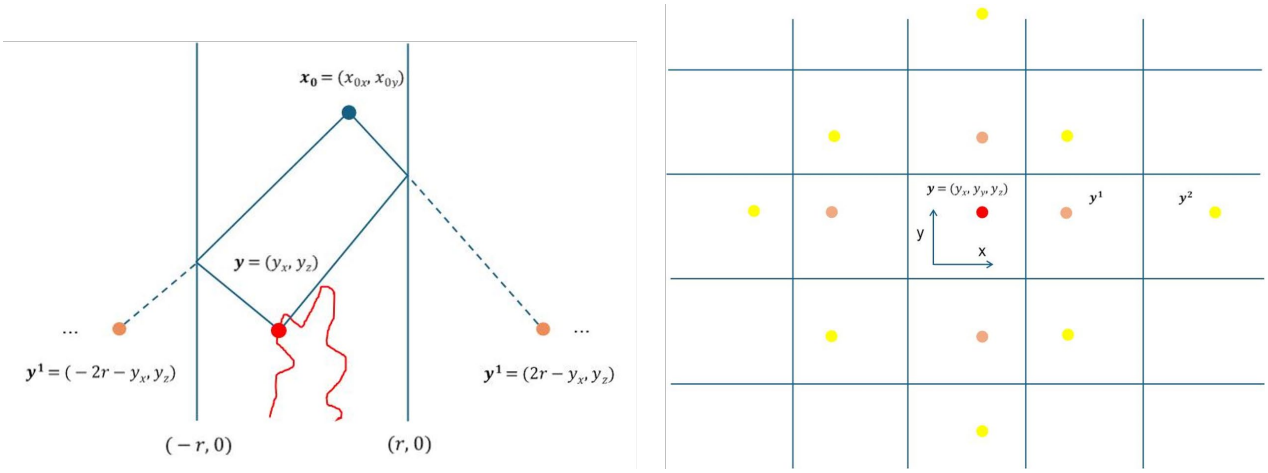

Figure 25. Illustration of the image source method for a 2D duct (left) and 3D duct viewed from above (right).

Analysis of Entropy Production Mechanisms

The objective of this task is to identify the dominant source terms in entropy production for accurate and flexible modeling of indirect combustion noise analysis of premixed and non-premixed flames. Prior work by our team on premixed flames has convincingly shown that fluctuations in heat-release dominate entropic fluctuations and hence indirect noise. However, in the case of non-premixed flames, where diffusion processes control the evolution and dynamics of the flame, the model requires rigorous analysis on other potential sources of entropy. In this reporting period, we have extended our entropy budget analysis framework to capture differential diffusion effects of species on entropy production due to mass diffusion. In our previous analysis, we were able to convincingly show the dominant effects of mass diffusion on producing significant amounts of entropy in a non-premixed turbulent flame (Sandia-D) and further analyzed the sensitivity of various production terms to operating conditions. Based on the feedback we received from our SciTech 2025 presentation, we have removed the problematic unity Lewis number, constant as well as equal mass diffusivities for all the species assumptions and thus incorporated the kinetic theory model in the calculations of species' diffusion coefficients. The mathematical formulation is presented below, and the preliminary results are discussed.

The governing equation of entropy transport in reacting, multicomponent flows is derived from the principles of energy conservation and the fundamental Gibbs relation as shown below:

$$\rho T \frac{Ds}{Dt} = -\nabla \cdot \vec{q} + \bar{\tau} : \nabla \vec{u} - \rho \sum_{i=1}^{N_s} D_i \nabla Y_i \cdot \vec{F_i} - \sum_{i=1}^{N_s} \mu_i \left(\dot{\omega}_i + \nabla \cdot (\rho D_i \nabla Y_i) \right) \quad \text{(Eq. 11)}$$

where ρ is density, T is temperature, $\bar{\tau}$ is the shear stress tensor and is modeled using Stokes' hypothesis, $\vec{u}$ is the velocity, D_i and Y_i is the laminar diffusion coefficient and mass fraction of species i, $\vec{F_i}$ is the body force per mass acting on species i, μ_i is the chemical potential of species i, $\dot{\omega}_i$ is the species production rate due to chemical reaction and $\frac{D}{Dt}$ is the substantial derivative. The heat flux vector $\vec{q}$ is given by:

$$\vec{q} = -k\nabla T + \quad \rho \sum_{i=1}^{N_s} h_i Y_i \vec{u}_{D,i} + R_u T \sum_{i=1}^{N_s} \sum_{j=1}^{N_s} \frac{X_j D_{T,i}}{W_i D_{ij}} \left(\vec{u}_{D,i} - \vec{u}_{D,j} \right) + \vec{q}_{rad} \quad \text{(Eq. 12)}$$

where h_i is the specific enthalpy of species i, $\vec{u}_{D,i}$is the diffusion velocity of species i, $D_{T,i}$ is the thermal diffusion co-efficient and D_{ij} is the binary mass diffusion coefficient of species i in otherwise pure j, $\vec{q}_{rad}$ is heat transfer due to radiation. The chemical reaction term $-\sum_{i=1}^{N_s} \mu_i \dot{\omega}_i$ can be further expanded as:

$$-\sum_{i=1}^{N_s} \mu_i \dot{\omega}_i = -\sum_{i=1}^{N_s} h_{f,i}^0 \dot{\omega}_i - \sum_{i=1}^{N_s} \dot{\omega}_i \int_{T_0}^{T} c_{p,i}\, dT + \sum_{i=1}^{N_s} T s_i \dot{\omega}_i = \dot{q} - \sum_{i=1}^{N_s} \dot{\omega}_i \int_{T_0}^{T} c_{p,i}\, dT + \sum_{i=1}^{N_s} T s_i \dot{\omega}_i \quad \text{(Eq. 13)}$$

where $\dot{q}$ is the HRR, $\sum_{i=1}^{N_s} \dot{\omega}_i \int_{T_0}^{T} c_{p,i}\, dT$ is the sensible enthalpy change of species i due to chemistry and $\sum_{i=1}^{N_s} T s_i \dot{\omega}_i$ is the partial entropy term.

The source terms on the right-hand side of Equation 11 represent entropy production due to heat flux, compressibility effects, body force, and chemical reactions respectively. Further, from the expansion of the heat flux vector, entropy is produced due to Fourier's heat conduction, enthalpy transport, full multicomponent diffusion, and radiation, respectively. Moreover, chemical reaction term represents the combined entropy generation due to heat release, sensible enthalpy changes, and partial entropy through species production/consumption. In the current extended framework, a simplified form of transport equation (Equation 11) is still considered by making a few assumptions in the context of low subsonic turbulent reacting flows. Assuming that the heat flux is driven purely due to heat conduction, only the first term on the right-hand side of Equation 12 is considered. For low subsonic flows, i.e., $M \ll 1$, compressibility effects are neglected and thus retaining only the viscous dissipation term. Second order diffusion effects such as Soret and Dufour diffusion are negligible in turbulence dominated flows and thus are neglected. In this extended model, the mass diffusion term is represented by Fickian diffusion, and the mass diffusion coefficients are calculated from kinetic theory, enabling us the riddance of unity Lewis number assumption. The diffusive mass flux is modeled using the mixture-averaged approach as:

$$J_i^{\alpha} = -\rho D_{\alpha,m} \nabla Y_{\alpha} \quad \text{(Eq. 14)}$$

Where Y_{α} is the mass fraction of species α, and the mixture-averaged diffusion coefficient $D_{\alpha,m}$ is defined as:

$$D_{\alpha,m} = \frac{1-X_\alpha}{\sum_{j\neq\alpha}\frac{X_j}{D_{\alpha,j}}} \quad \text{(Eq. 15)}$$

From Chapman-Enskog model for species diffusivity, the binary diffusion coefficient $D_{\alpha j}$ is calculated as follows:

$$D_{\alpha j} = \frac{3\kappa_B T\sqrt{\frac{4\pi\kappa_B T}{M_{\alpha j}}}}{16P\pi\sigma_{\alpha j}^2\Omega_D(T^*)} \quad \text{(Eq. 16)}$$

Incorporating the above assumptions and model changes, the resulting simplified entropy transport equation analyzed in this study is given as follows:

$$\frac{\partial\rho s}{\partial t} + \frac{\partial\rho u_i s}{\partial x_i} = \frac{\partial^2 s}{\partial x_i^2} + \frac{1}{T}\tau_{ij}\frac{\partial u_i}{\partial x_j} - \frac{\rho}{T}\sum_{\alpha=1}^{N_s}\mu_\alpha S_\alpha - \sum_{\alpha=1}^{N_s} J_i^\alpha \frac{R_\alpha}{X_\alpha}\frac{\partial X_\alpha}{\partial x_i} + \frac{\kappa}{T^2}\frac{\partial T}{\partial x_i}\frac{\partial T}{\partial x_i} \quad \text{(Eq. 17)}$$

In this simplified form of transport equation, the first term on the right-hand side represents the diffusion of entropy while the rest of the terms represent the volumetric entropy production rate due to viscous dissipation, heat conduction, mass diffusion, and chemical reaction, respectively.

To test this model, we have performed large eddy simulations on the Sandia-D flame like our prior work.
The computational domain of dimensions $100\ \ d_j \times 100\ \ d_j \times 105\ \ d_j$, where d_j is the jet-diameter of 7.2 mm, is used for the Sandia-D flame as shown in Figure 26.

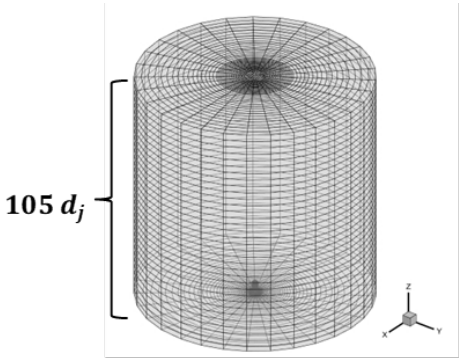

Figure 26. Computational domain of the Sandia-D flame.

As the flame is unconfined, the co-flow inlet of air spans $48\ d_j$ on either side of the jet-inlet. The length of the burner is $5\ d_j$ measured upstream of the jet exit as shown in Figure 26. The flame is stabilized by defining a pilot mixture of hot products of ethyne-air mixture at equivalence ratio of 0.77, spanning $2.5\ \mathrm{d_j}$. The summary of the boundary conditions is provided in Table 3.

Table 3. Boundary conditions of the baseline Sandia-D flame.

Condition	Jet	Pilot	Co-flow
Velocity (m/s)	49.6	11.4	0.9
Temperature (K)	294	1880	291
Pressure (atm)	0.993	0.993	0.993
Y_{CH_4}	0.156	0	0
Y_{O_2}	0.197	0.054	0.233
Y_{CO_2}	0	0.11	0
Y_{H_2O}	0	0.0942	0
Y_{CO}	0	4×10^{-3}	0
φ	2.38	0.77	0

The simulation for Sandia-D flame was performed using Ansys® Fluent 2024 R1 solver. The Wall adapting local eddy-viscosity (WALE) model is used for closure of the sub filter unresolved source terms in the LES equations. Detailed chemistry with pure finite rate effects has been used for modelling the chemical reactions for the Sandia-D flame. The chemical mechanism consists of 16 species and 41 reactions. Species transport model with Stiff Chemistry solver has been used to solve the species' conservation equations. Further, to isolate the pure transport effects, no turbulence-chemistry interaction was modeled. The equations are discretized using a cell-centered finite volume co-located pressure-based segregated solver. The pressure-velocity coupling is achieved using a SIMPLEC predictor-corrector algorithm. The numerical scheme is second-order accurate in space, and a bounded second-order implicit scheme is used for transient formulation. For accurate prediction of the material properties of the species, temperature dependent models like piecewise-polynomial and Sutherland formulations are used for computing specific heat and viscosity, respectively. Mass diffusivity is modeled using the kinetic theory model. Mixing law models are used for calculating the mixture-averaged properties. The entropic source-terms were calculated using a user-defined scalar formulation by treating the production of entropy as a passive scalar in the solution. Additionally, the source terms were volumed averaged locally to filter out the spatial fluctuations. For the transient calculation of both the flames, the Courant-Friedrichs-Lewy (CFL) value of 0.8 was maintained with the time-step size of 25 μs. The simulation was first run for 10 flowthroughs to wash out initial transient effects, after which statistical data were collected for an additional 15 flowthroughs for the final analysis.

First, the qualitative representations of entropy production in the Sandia-D flame due to different sources are discussed, Figure 27 shows the qualitative trends of time-averaged volumetric entropy production rates due to viscous dissipation, heat conduction, mass diffusion, and chemical reaction respectively at the center-plane. Consistent with the trends we have observed previously, the effects of viscous dissipation and heat conduction are highly negligible as seen from the orders of magnitude differences with the effects of mass diffusion and chemical reaction, respectively. The effects of mass diffusion and chemical reaction are still the dominant sources of entropy production rates. Species' concentration gradients drive mass diffusion and as the overall effect is summed over all the species, the resulting entropy production is significant. It can also be seen that as the flame grows downstream, forming an over-ventilated flame eventually, the regions of intense species production/consumption increase, thus resulting in wider species radial gradient profiles, and larger entropy production rates. Chemical reaction term is dominated by the species' production rates, and the associated entropy production rates are significant around the flame region. Moreover, as the overall effect is summed over all the species' production/consumption rates, the resulting entropy production is significant. The absolute magnitude of the mass diffusion contribution is higher than that of the chemical reaction, indicating the shortcomings of our previous model. The spatial profiles of integrated production rates across the flame are presented and contrasted with the results from the previous model next.

® Ansys is a registered trademark of Ansys, Inc., Canonsburg, Pennsylvania.

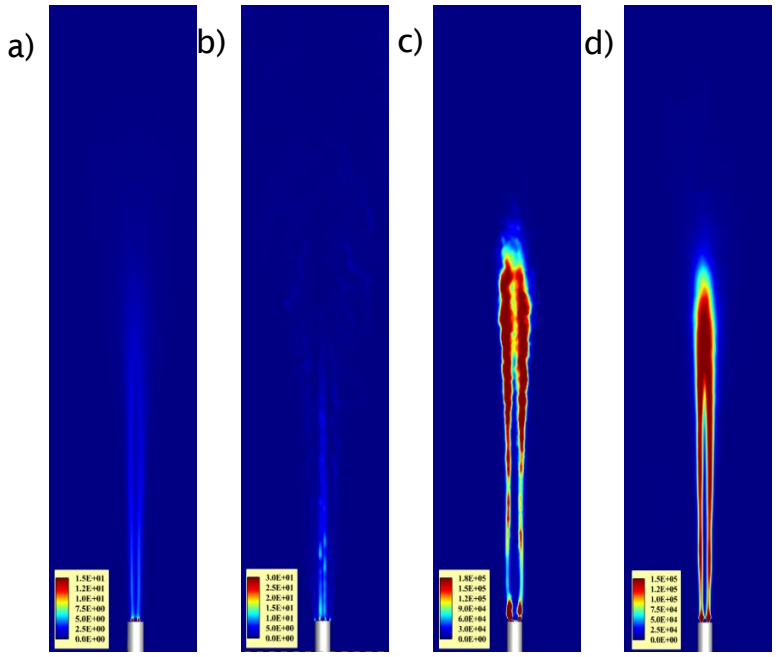

Figure 27. Qualitative representation of entropy production rates (J/K/m^3-s) in the center-plane (x=0) due to (a) viscous dissipation, (b) heat conduction, (c) mass diffusion, and (d) chemical reaction.

Figure 28 shows the integrated entropy production rate distribution due to various sources across the flame. As expected, the integrated entropy production due to viscous dissipation (blue line) and heat conduction (green line) are negligible across the flame. However, the updated mass diffusion term (solid black dots) appears to produce significant amounts of entropy, dominating the effect of chemical reactions (solid red line). This is a very significant observation in the context of indirect noise, as strong differential diffusion effects can lead to strong entropic fluctuations.

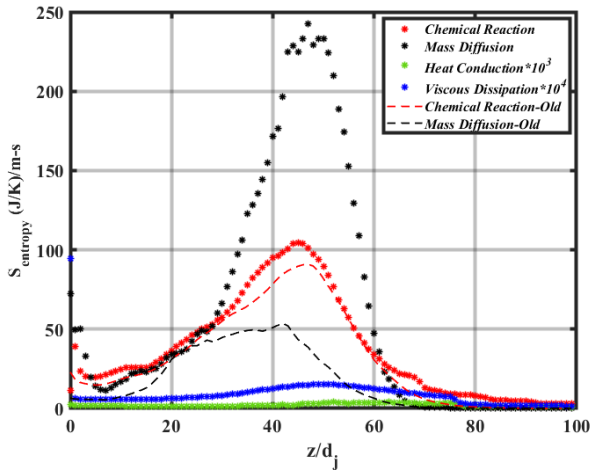

Figure 28. Spatial distribution of integrated mean entropy production rates (J/K/m-s) across the flame. Dashed lines correspond to results from the previous model.

Next, we are planning to rigorously analyze the sensitivity of these different source terms for various conditions using the canonical flame set-ups. Since the calculations involve computations of several gradients, a grid sensitivity analysis will be performed to verify the above observations. Additionally, the entropy budget analysis will be performed on an industrial-scale combustor configuration at elevated conditions to ascertain the trends observed from canonical flame configuration simulations.

Milestones

- Test validation strategies for global stability modeling by implementation of data-driven POD techniques.
- Extended p-q coherence study to 3D square ducts.
- Improved analysis of entropy budget completed based on relaxing earlier assumptions.

Major Accomplishments

Unsteady, spatio-temporal LES data were used by the hydrodynamics team to evaluate leading POD hydrodynamic modes including their dynamical frequencies and mode-shapes. Coherence modeling study showed differences in considering a 3D configuration versus 2D configuration. Entropy budget analysis framework can now consider more detailed molecular transport models.

Publications

Published Conference Proceedings

Patki, P. A., Ek, H., Acharya, V., & Emerson, B. L. (2025, March 16-19). *Reduced order modeling and validation of hydrodynamic modes of reacting, swirling jets.* 14th U.S. National Combustion Meeting, Boston, Massachusetts.

Ganesh, G.C., Ansari, N., Orsino, S., Xia, Y., & Acharya, V. (2025, January). *Analysis of Entropy Production Mechanisms in Turbulent Diffusion Flames.* AIAA SciTech Forum 2025, Orlando, Florida.

Outreach Efforts

None.

Awards

None.

Student Involvement

- Graduate student Parth Patki worked on the hydrodynamic stability task under the mentoring of Ben Emerson.
- Graduate student Sungyoung Ha worked on the coherence modeling task under the mentoring of Vishal Acharya and Tim Lieuwen.
- Graduate student Guru Charan Ganesh worked on the entropy generation task under the mentoring of Vishal Acharya.

Plans for Next Period

- Use RTRC tone campaign data for addition to flame response modeling validation.
- Consider advanced modal decomposition techniques for improved secondary validation and improvement of Tri-Global model from previous year with conclusions of the primary validation study.
- Build reduced order modeling for entropy noise based on findings from current reporting period.

Task 4 – Facility Development

RTX Technologies Research Center

Objective

The objective of this task is to provide machine learning data for combustion instability over range of configurations and operating conditions.

Research Approach

The combustor rig for the tone campaign test is shown in Figure 29 (left) together with the original test arrangement that was used for the broadband noise campaign (right). The tone campaign rig was achieved by removing the jail bars section, replaced with a constant area section. The VRASC section with a variable length side branch and variable elliptic choke was installed downstream of the combustion section. The side branch length of the VRASC tube varied by the plunger location.

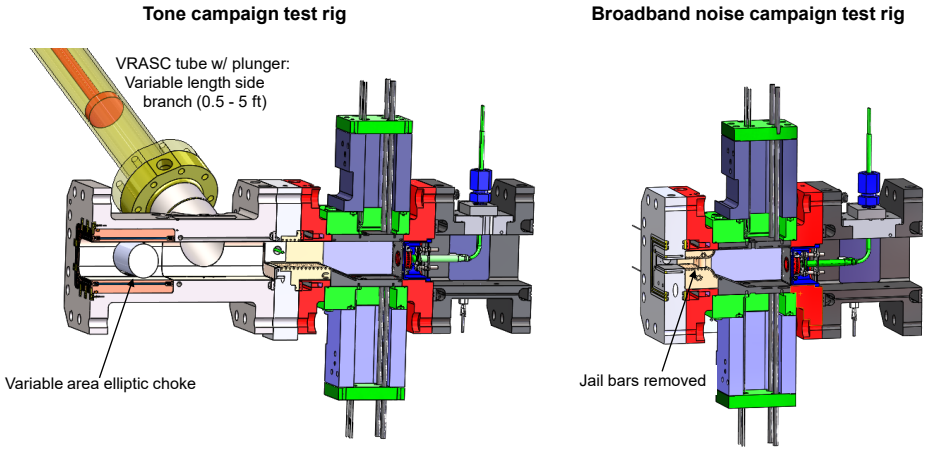

Figure 29. Test combustor rig for tone campaign vs original ASCENT combustor rig for broadband noise.

The dynamic instrumentation is shown in Figure 30 which consists of three diagnostics:

1. A photodiode sensor that captures a focused, time resolved chemiluminescence (OH*) signal of the unsteady combustion, which is a surrogate of the Unsteady Heat Release (UHR), and is used to compute Rayliegh gain,
2. Dynamic pressure tap array for wave decomposition and estimate of indirect noise, and
3. A dual thermocouple (dual TC) for temperature fluctuations downstream of the combustion.

In addition, several other locations (e.g., bulkhead) were instrumented for dynamic pressure, the bulkhead and other locations are illustrated in the figure on the right side of Figure 30.

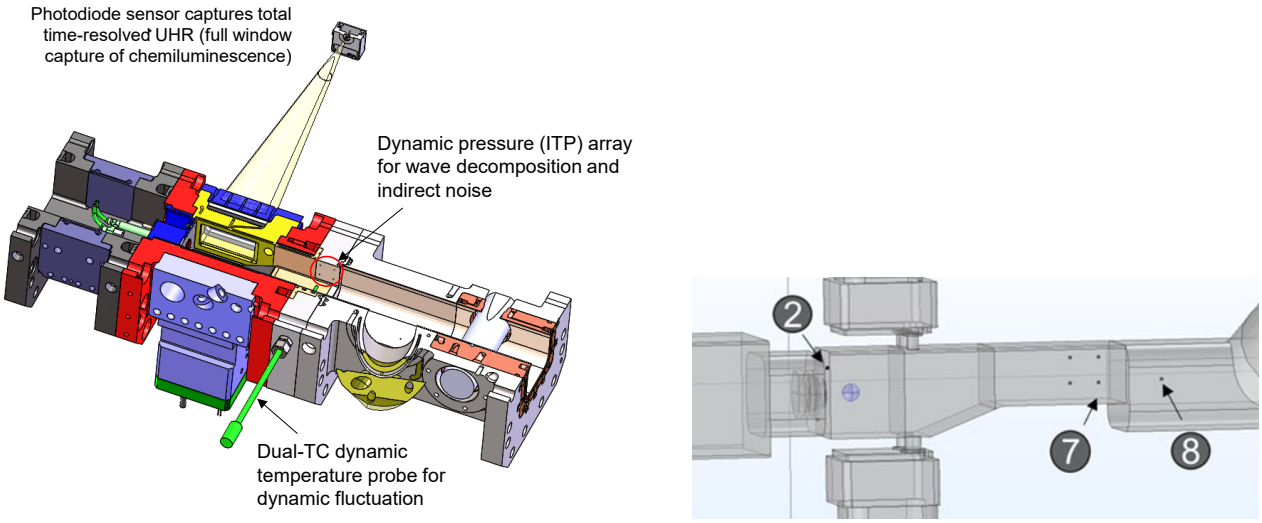

Figure 30. Dynamic instrumentation for test rig shown using the CAD drawing on the left and using the COMSOL Multiphysics model setup on the right.

The immersion of the fuel nozzle in the swirler (air-fuel mixer) was variable for this test campaign. Three immersions were tested and are shown in Figure 31.

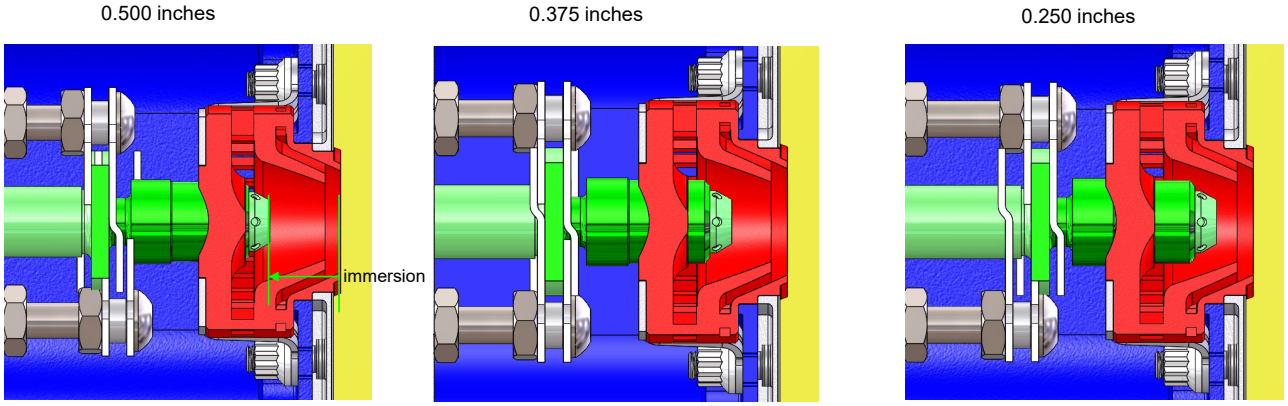

Figure 31. Fuel mixer configurations tested.

The test matrix focused on approach and ground Idle conditions. The target conditions are shown in Figure 32. Due to very high combustion dynamics (i.e., high pressure fluctuations), the initial two test days had limited conditions acquired because of concerns with rig health.

		Data Point Number	
Immersion	**0.25**	**0.5**	**0.375**
Description	**6/30/25**	**7/7/25**	**7/11/25**
Apprch: Cycle Pt. @ Cycle Cond.	**6**	**4**	**6**
Apprch: FARtot_+1up	**8**	**8**	**8**
Apprch: FARtot_+2up	**10**	**10**	**10**
Apprch: FARtot_+3up (HOT TCs)	**14**	**14**	
Apprch: FARtot_-1down	**16**	**16**	**12**
Apprch: Cycle Pt. @ T3 = 600 F	**18**	**22**	**18**
Apprch: FARtot_+1up	**20**	**24**	**16**
Apprch: FARtot_+3up	**26**	**26**	**14**
Apprch: FARtot_+4up (HOT TCs)		**28**	
Apprch: Cycle Pt. @ T3 = 500 F		**30**	**20**
Apprch: FARtot_+1up		**32**	**22**
Apprch: FARtot_+3up			
Apprch: FARtot_+4up			
Apprch: FARtot_+5up (HOT TCs)			
App Pt. @ T3=500 F, FAR+1, 20pph			**24**
Apprch: 500F, FAR+1, 40pph_Pilot			**26**
Apprch: 500F, FAR+1, 60pph_Pilot			**28**
Apprch: 500F, FAR+1, 80pph_Pilot			
App Pt. @ T3 = 500 F, FAR+1, 28/46			**30**
Apprch: 500F, FAR+1, 30/44=SwBH/Q			**32**
Apprch: 500F, FAR+1, 32/42=SwBH/Q			**34**
G-Idle: Cycle Pt.			**44**
G-Idle: FARtot_2			**42**
G-Idle: FARtot_3			**40**
G-Idle: FARtot_4			**38**
G-Idle: FARtot_5			**36**

Figure 32. Test matrix.

For each data point, dynamic data were acquired in a continuous manner as the VRASC plunger was swept from one end of its range to the other end (stoke range: 6 to 54 in.) over the course of 190 s. A typical combustion dynamic pressure response is shown in Figure 33 in terms of a spectrogram in plunger stroke vs frequency. As can be seen in the figure, the combustion instability tracks along the longitudinal modes (i.e., standing wave between bulkhead [BH] and plunger face) over a frequency range, in this case from 570 -720 Hz. As the plunger proceeds to longer stroke positions, the instability will jump from a lower longitudinal mode to the next higher mode to maintain this frequency range, thus identifying the dynamic characteristic of the fuel mixer. To characterize the response for a given immersion and operation point, the peak dynamic pressure and associated frequency are identified which is shown by the black circle in the spectrogram, location just above 600 Hz and the 20 in Stroke position. The specific value of peak-to-peak dynamic pressure and frequency are listed in the figure title.

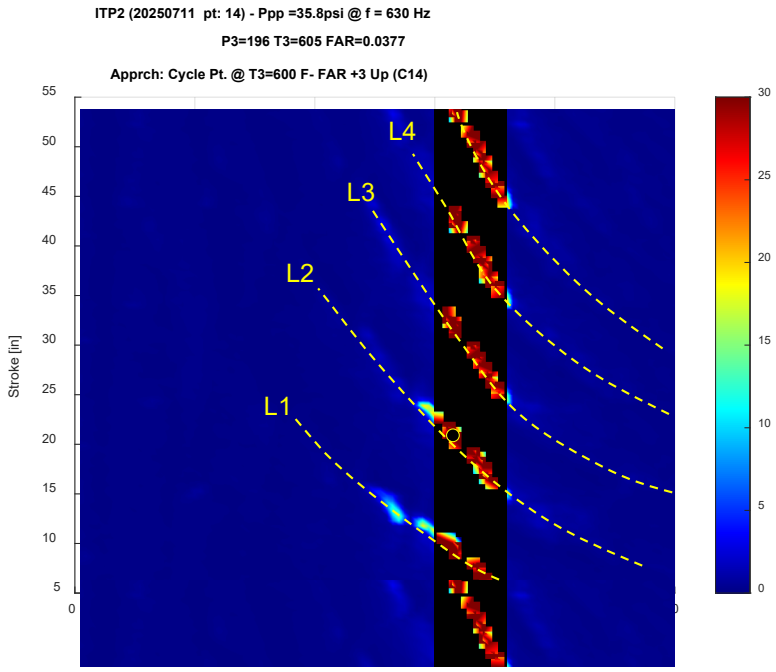

Figure 33. Typical dynamic pressure spectrogram for one operational condition. FAR: fuel-air ratio.

Figure 34 plots a summary of the peak response data versus FAR sweeps and the bulkhead pressure sensor. The top row is the pressure amplitude (half peak-to-peak value) and bottom row is the associated frequency. The cycle condition is listed at the top of each column, and the immersion configuration is identified by the symbol color.

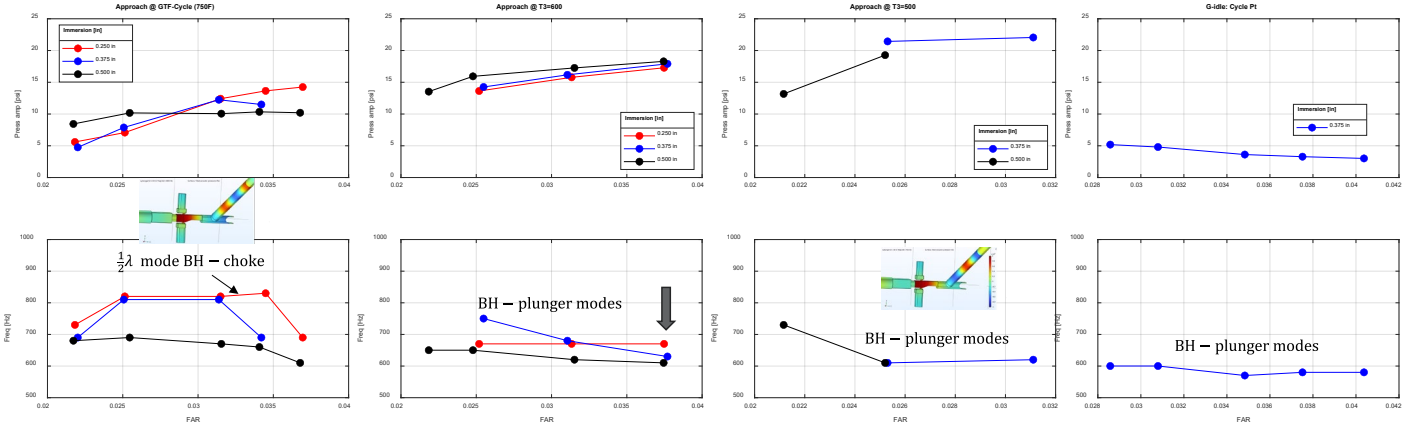

Figure 34. Summary of peak dynamic pressure and associated frequency.

As noted on the frequency plots, for five points (see Approach @ GTF-cycle [750°F]), the frequency is associated with a BH-choke half wave-length mode. For this mode, the BH-plunger and BH-choke modes are matching which causes (as the modeling shows) the acoustic pressure generated by a given combustor unsteadiness to be the largest here, making the attraction to instability much greater than the BH-plunger mode alone. Hence, these responses are of limited interest since they limit the range of the frequency response. More specifically, the bands of response shown in Figure 33, are mainly vertical along the 800 Hz frequency.

For the Approach @ T3=600°F conditions, the data here provide the more comparative assessment of the three immersion configurations. Unlike previous experience with more engine relevant fuel mixers that show great sensitivity to immersion, the results here do not. This is attribution to the large Acd (effective flow area) of the current fuel mixer and the limited number of outer flow passages (2). For the detailed dynamic analysis of Rayliegh gain and indirect noise estimation, the effort was focused on these conditions as identified in the figure.

For the detailed dynamic analysis, a good finite-element analysis (FEA) model is needed. The model domain and applied temperatures (mainly based on measured operating conditions together with adiabatic flame model) is shown in **Figure 35**. The primary data-matching parameter is the temperature of gas at the plunger face which was found to depend on stroke position.

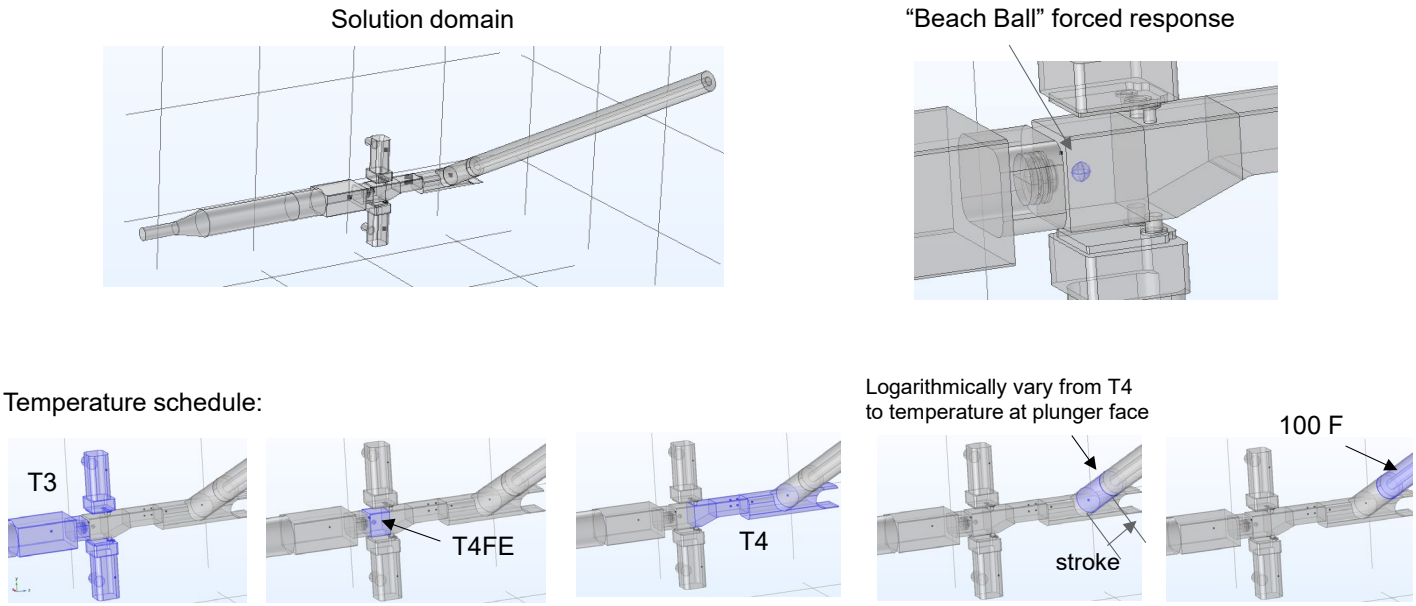

Figure 35. Finite element acoustic model using pressure-acoustics solver in COMSOL Multiphysics software.

The validation comparison of model vs data is shown in Figure 36 which compares the pressure ratio from a combustor aft dynamic pressure position (#8) to the BH (#2). Comparison is very good, capturing the BH-plunger longitudinal modes as well as the modes behind the "leaky" plunger. Quantifying line plots also confirm excellent data matching.

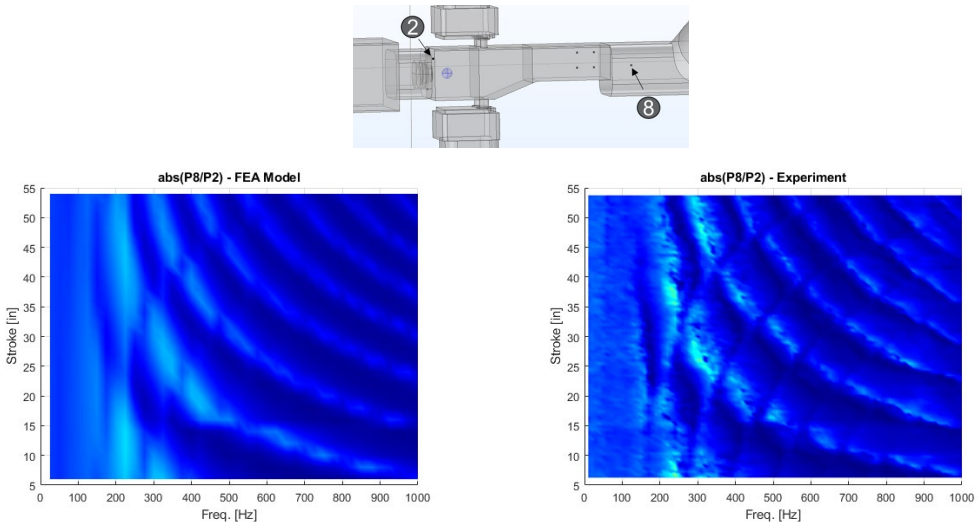

Figure 36. Comparison of data vs. model for full stroke variation.

Rayliegh gain was computed using the Eigenvalues from the FEA combined with the measure unsteady chemiluminescence. Rayliegh gain is shown in the approximate acoustic equation shown in Figure 37 (η = normalized dynamic pressure and ψ is the acoustic mode shape) and is the driving mechanism of combustion instability.

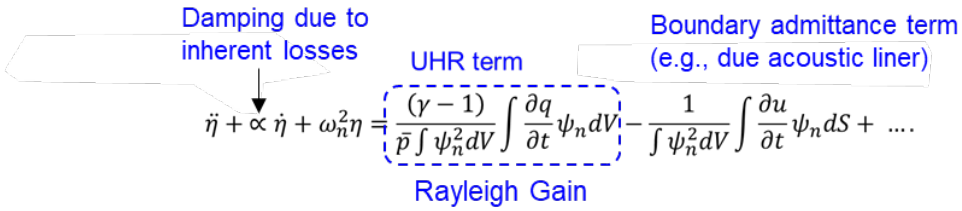

Figure 37. Rayliegh gain equation.

In a first attempt to characterize the Rayliegh gain vs plunger location, a FEA model was developed in COMSOL Multiphysics software to integrate the UHR with the acoustic modes. Figure 38 shows graphically the outline of the approach.

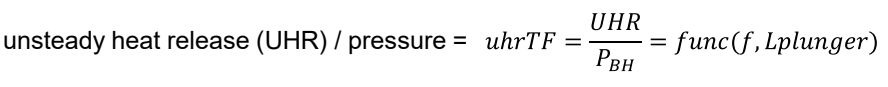

unsteady heat release (UHR) / pressure = $uhrTF = \frac{UHR}{P_{BH}} = func(f, Lplunger)$

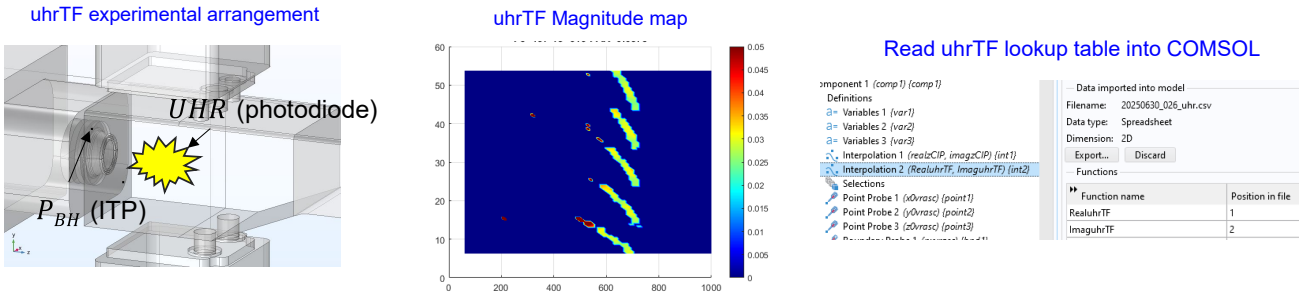

Compute UHR for each mode and integrate p*UHR over combustion volume = Rayleigh Gain

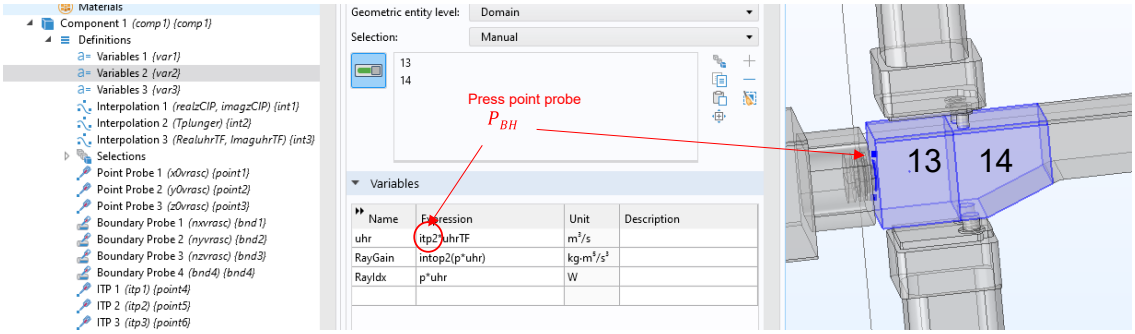

Figure 38. Approach to estimate Rayliegh gain from chemiluminescence data and FEA model.

Before showing the Rayliegh gain results, it is helpful to understand the modal content in the test rig. With the FEA model, the Eigenvalues were computed at half-inch increments of the plunger location. Approximate 20 were found around the band of interest (200-1,000 Hz). Shown in Figure 39 (left plot) is all the Eigenvalues that were discovered. To sort out the ones of interest, the volume-averaged mode shape (Λ) in the blue domain (combustion zone) was computed (color of dot). By picking a limit of Λ of 0.5, the modes of interest in the combustion zone are easily identified (right-hand plot). The gray lines are hand-faired lines from plots on the left which track the modes behind the plunger. The impact of these modes is visible in the right-hand plot.

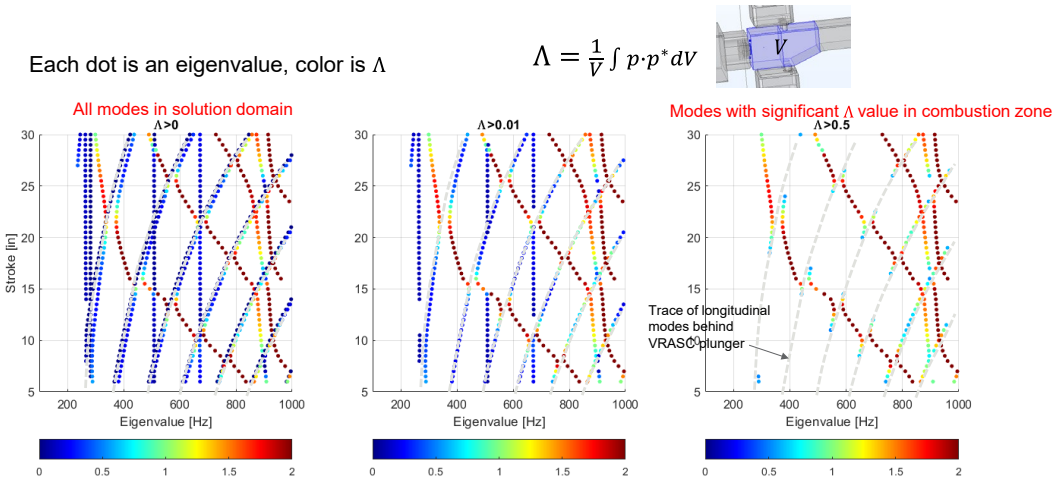

Figure 39. Acoustic Eigenvalues (dots) for one operating condition for full stroke variation and volume averaged mode shape in combustion region (Λ=color).

Figure 40 shows the Rayleigh gain results for the three immersion cases for the approach condition (T3=600 F), FAR excursion. The plots below show the modes with $\Lambda > 0.5$ colorized by the magnitude of the Rayliegh gain. The deeper the color red is, the greater the gain and hence the dynamic pressure. These results are consistent with the trending of measured dynamic pressure (increased immersion increases the dynamic pressure amplitude and lowers the associated frequency. This analysis represents a first for the VRASC tone rig and is a valuable tool to assess future fuel mixer investigations.

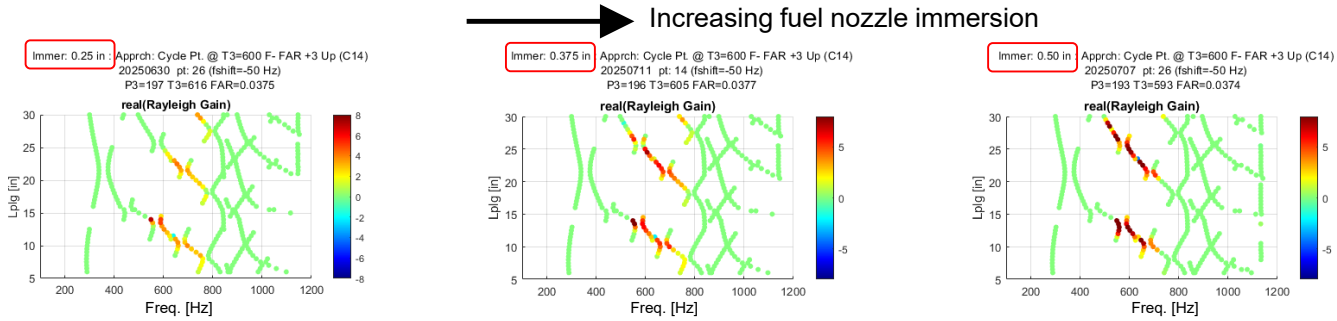

Figure 40. Rayleigh Gain maps verses immersion.

Figure 41 shows the result of the indirect noise estimate. This approach has been described in previous annual reports. In brief, when entropy/temperature fluctuation from the combustion process convect downstream through the choke, noise is generated that travel both downstream and upstream. Using the dynamic pressure array shown in Figure 30, the acoustics can be decomposed into downstream (A component) and upstream traveling (B component). By comparing the Bexp component from the test with the Bmodel component from the FEA (with does not contain indirect noise), the indirect noise can be estimated from the difference, Bexp-Bmodel. For the same conditions shown in Figure 40 for the Rayliegh gain, the estimated indirect noise spectrogram are shown in Figure 41. These results are consistent with the measured dynamic pressure data in that increased immersion corresponds with increased noise. Also interesting is the spottiness at lower frequencies suggesting temperature fluctuation in this band that is more significant for the larger immersion. This is in fact the observation from the temperature measurements (not shown).

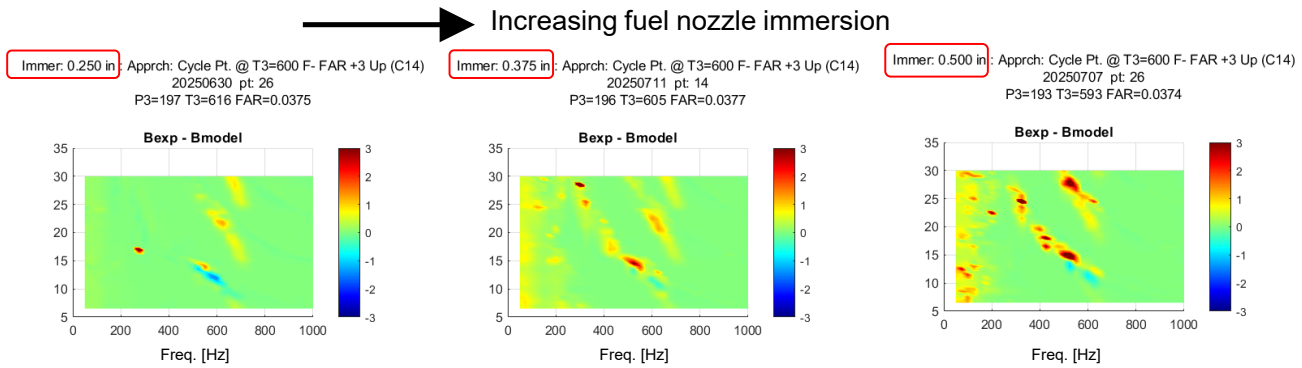

Figure 41. Estimated indirect noise variation with immersion.

In summary, though sensitivity to immersion in this campaign was less than expected, three new diagnostic techniques (Rayliegh gain, indirect noise, and d/s temperature fluctuations) for combustion tone studies have been developed and shown to be consist with observed dynamic pressure trending and should be a useful tool for future tone investigations. The Rayliegh gain estimation will be further refined and developed in the next phase of funding. Results shown here show great promise as a diagnostic tool. The following summarizes accomplishments and next steps for this effort.

Milestones

- Completed Year 1 Tone Prominence Program, RTRC main task a rig test identifying tone instabilities.
- Obtained initial GT rig LES results identifying peak mode at frequency consistent with rig test.

Major Accomplishments

- Demonstrated new VRASC rig diagnostics for dynamic analysis: dynamic exit temperature mapping, indirect noise mapping, UHR, and Rayleigh gain mapping.

Publications

None.

Outreach Efforts

None.

Awards

None.

Student Involvement

None.

Plans for Next Period

- Further develop Rayleigh gain analysis (integration of UHR and acoustic modes) as current development shows much promise (planned next phase, Year 2)
- Year 2 proposed, waiting for FAA to award.
  - Continue initial validation of GT LES with RTRC data (Y1),
  - Match rig LES and data at multiple rig test conditions (Y2),
  - Refine stability analysis (Y2), leverage LES/test for ML to define HRR ROM (Y2), Initiate analysis for design low tone design (Y2).
  - This program, when completed, will provide insight into instability challenges (prediction and mitigate) and a framework for propagating tones through the turbine and into the far field for noise.